

1 **NEMO reshapes the protein aggregate interface and promotes aggrephagy by co-**
2 **condensation with p62**

3

4 Nikolas Furthmann¹, Lena Angersbach^{1#}, Verian Bader^{1,2#}, Alina Blusch^{3#}, Simran Goel¹, Ana
5 Sánchez-Vicente¹, Laura J. Krause^{1,4}, Prerna Grover², Victoria A. Trinkaus⁵, Eva M. van
6 Well¹, Maximilian Jaugstetter⁶, Kristina Tschulik^{4,6}, Rune Busk Damgaard⁷, Carsten Saft³,
7 Gisa Ellrichmann^{3§}, Ralf Gold³, Arend Koch⁸, Benjamin Englert^{8§§}, Markus Glatzel⁹, F. Ulrich
8 Hartl^{5,10}, Ken Nakamura^{11,12}, Chadwick W. Christine^{11,13}, Eric J. Huang^{13,14}, Jörg Tatzelt^{2,4} and
9 Konstanze F. Winklhofer^{1,4*}

10

11 ¹Department Molecular Cell Biology, Institute of Biochemistry and Pathobiochemistry, Ruhr
12 University Bochum, 44801 Bochum, Germany.

13 ²Department Biochemistry of Neurodegenerative Diseases, Institute of Biochemistry and
14 Pathobiochemistry, Ruhr University Bochum, 44801 Bochum, Germany.

15 ³Department of Neurology, St Josef Hospital, Ruhr University Bochum, 44791 Bochum,
16 Germany.

17 ⁴Cluster of Excellence RESOLV, 44801 Bochum, Germany.

18 ⁵Department of Cellular Biochemistry, Max Planck Institute of Biochemistry, 82152
19 Martinsried, Germany.

20 ⁶Analytical Chemistry II, Faculty of Chemistry and Biochemistry, Ruhr University Bochum,
21 44801 Bochum, Germany.

22 ⁷Department of Biotechnology and Biomedicine, Technical University of Denmark, 2800
23 Kongens Lyngby, Denmark

24 ⁸Charité - Universitätsmedizin Berlin, Corporate Member of Freie Universität Berlin and
25 Humboldt-Universität zu Berlin, Department of Neuropathology, Charitéplatz 1, 10117, Berlin,
26 Germany.

27 ⁹Institute of Neuropathology, University Medical Center Hamburg-Eppendorf, Martinstraße
28 52, 20251 Hamburg, Germany.

29 ¹⁰Munich Cluster for Systems Neurology (SyNergy), 81377 Munich, Germany

30 ¹¹Department of Neurology, University of California, San Francisco, California, USA.

31 ¹²Gladstone Institute of Neurologic Disease, San Francisco, California, USA.

32 ¹³Weill Institute for Neurosciences, University of California San Francisco, San Francisco
33 California, USA.

34 ¹⁴Department of Pathology, University of California, San Francisco, California, USA.

35

36 #Equal contribution

37 *Corresponding author: Konstanze F. Winklhofer, Email: konstanze.winklhofer@rub.de

38

39 §Current address: Department of Neurology, Klinikum Dortmund, University Witten/Herdecke,
40 44135 Dortmund, Germany

41 §§Current address: Center for Neuropathology and Prion Research, Ludwig-Maximilians
42 University, 81377 Munich, Germany

43

44

45

46 **ABSTRACT**

47 NEMO is a ubiquitin-binding protein which regulates canonical NF- κ B pathway activation in
48 innate immune signaling, cell death regulation and host-pathogen interactions. Here we
49 identified an NF- κ B-independent function of NEMO in proteostasis regulation by promoting
50 autophagosomal clearance of protein aggregates. NEMO-deficient cells accumulate misfolded
51 proteins upon proteotoxic stress and are vulnerable to proteostasis challenges. Moreover, a
52 patient with a mutation in the NEMO gene resulting in defective binding of NEMO to linear
53 ubiquitin chains, developed a widespread mixed brain proteinopathy, including α -synuclein,
54 tau and TDP-43 pathology. NEMO amplifies linear ubiquitylation at α -synuclein aggregates
55 and promotes the local concentration of p62 into foci. In vitro, NEMO lowers the threshold
56 concentrations required for ubiquitin-dependent phase transition of p62. In summary, NEMO
57 reshapes the aggregate surface for efficient autophagosomal clearance by providing a mobile
58 phase at the aggregate interphase favoring co-condensation with p62.

59

60

61 **INTRODUCTION**

62 Cellular proteostasis is maintained by an elaborate network of protein quality control
63 components, such as molecular chaperones, the ubiquitylation machinery, the proteasome
64 and the autophagy-lysosome pathway, to coordinate the proper triage, subcellular quarantine,
65 and refolding or disposal of damaged proteins. In aging, proteotoxic stress along with a decline
66 in the fidelity of protein quality control favors the accumulation of misfolded proteins,
67 challenging the integrity of the cellular proteome. This is particularly relevant to postmitotic
68 cells, such as neurons. In fact, the age-dependent accumulation of misfolded proteins is a
69 characteristic feature of neurodegenerative diseases. Cells are equipped with two proteolytic
70 machineries, the ubiquitin-proteasome system and the autophagy-lysosomal system that
71 remove misfolded proteins depending on their subcellular localization, their structure,
72 oligomerization state and posttranslational modifications. Both degradation pathways are
73 critically regulated by ubiquitin in cooperation with specific ubiquitin-binding proteins that target
74 cargo to the proteasome or to selective autophagy^{1, 2, 3, 4, 5, 6}. Ubiquitylation is a highly elaborate
75 posttranslational modification, regulating a plethora of cellular processes. Its complexity is
76 based on different variables, such as the number of ubiquitin molecules attached to substrates,
77 the mode of inter-ubiquitin linkage, the formation of homo- and heterotypic chains, and the
78 posttranslational modification of ubiquitin itself, for example by phosphorylation, SUMOylation,
79 or NEDDylation^{7, 8, 9, 10}. In conventional ubiquitination, the C-terminal glycine of ubiquitin is
80 linked to one of seven lysine residues of another ubiquitin molecule by an isopeptide bond.
81 Alternatively, the C-terminal glycine can be linked to the N-terminal methionine of the acceptor

82 ubiquitin, resulting in the formation of a peptide bond¹¹. This type of head-to-tail linkage is
83 called linear or M1-linked ubiquitylation. Linear ubiquitin chains are exclusively generated by
84 the RING-in-between-RING (RBR) E3 ubiquitin ligase HOIP, the catalytic component of the
85 linear ubiquitin chain assembly complex (LUBAC). Within this complex, HOIP interacts with
86 HOIL-1 and SHARPIN, which bind to the ubiquitin-associated (UBA) domain of HOIP by their
87 ubiquitin-like (UBL) domain, thereby activating autoinhibited HOIP^{12, 13, 14, 15, 16, 17, 18, 19, 20, 21}.
88 LUBAC has mostly been studied in the context of immune signaling, NF- κ B activation and cell
89 death regulation^{22, 23, 24, 25, 26}. In these paradigms, the regulatory component of the IKK (inhibitor
90 of κ B kinase) complex NEMO (nuclear factor- κ B essential modulator), also called IKK γ , is an
91 important player, serving both as an interactor of linear ubiquitin chains and a substrate of
92 HOIP^{27, 28, 29}. Binding of NEMO to M1-linked ubiquitin chains via its UBAN (ubiquitin-binding in
93 ABIN and NEMO) domain and also ubiquitylation of NEMO upon activation of innate immune
94 receptors, such as the TNF receptor 1, induces a conformational change in NEMO and
95 activates the associated kinases IKK α and IKK β ^{14, 30, 31}. The activated IKK kinases
96 phosphorylate I κ B α (inhibitor of κ B α), which is then modified by K48-linked ubiquitin chains
97 and degraded by the proteasome. Thereby, NF- κ B heterodimers, typically p65 and p50, are
98 liberated from their binding to I κ B α and translocate to the nucleus to regulate the expression
99 of NF- κ B-dependent genes.

100 Amorphic or hypomorphic mutations in the NEMO-encoding *IKBKG* gene located on the X
101 chromosome are associated with *Incontinentia pigmenti* (IP), a condition that is usually lethal
102 in male fetuses and thus almost exclusively occurs in female patients with mosaic X-
103 chromosome inactivation^{32, 33, 34}. IP is a rare multisystem disorder that primarily affects the
104 skin, but can also involve other ectodermal tissues including teeth, hair, nails, eyes and the
105 central nervous system³⁵. IP-linked mutations comprise rearrangements, nonsense,
106 frameshift, splice site, or missense mutations^{33, 34}. Although IP can be inherited in an X-linked
107 dominant fashion, between 65 and 75% of cases occur sporadically due to *de novo* mutations
108³⁶. The phenotypic heterogeneity of the clinical presentation is based on the fact that in each
109 tissue, cells expressing the wildtype *IKBKG* allele coexist with cells expressing the mutant
110 *IKBKG* allele, hampering the analysis of patients' biosamples and the establishment of patient-
111 derived cellular models. We identified a patient suffering from IP who developed early onset,
112 rapidly progressive neurodegeneration with a widespread mixed proteinopathy, including α -
113 synuclein, tau, and TDP-43 aggregates. The pathogenic Q330X NEMO mutant is
114 compromised in NF- κ B pathway activation, explaining the manifestation of IP, but in addition
115 causes defective protein quality control. NEMO deficiency favors the accumulation of
116 misfolded proteins and impairs the clearance of protein aggregates by autophagy. Our study
117 revealed a critical function of NEMO in proteostasis regulation by remodeling the aggregate
118 interface and facilitating condensate formation of the autophagy cargo receptor p62.

119

120 RESULTS

121 A pathogenic mutation in the *IKBKG* gene encoding NEMO is associated with a 122 widespread mixed proteinopathy and progressive neurodegeneration

123 A female patient, who was diagnosed with IP during her infancy, developed parkinsonism (left-
124 sided bradykinesia, hypophonia, slowed gait) at age 48. She noted initial benefit with treatment
125 with carbidopa/levodopa but her condition rapidly progressed, forcing retirement from work as
126 a school teacher at age 52. A dopamine transporter scan was markedly abnormal, showing
127 near absence of tracer uptake within the caudate and putamen bilaterally. She then developed
128 severe cognitive impairment and died at age 56 from progressive neurodegeneration. Brain
129 autopsy revealed a widespread mixed proteinopathy, including α -synuclein, tau, and TDP-43
130 aggregates with predominant α -synuclein pathology (Fig. 1A). There was no family history of
131 neurodegenerative diseases and exome sequencing did not identify mutations in common
132 Parkinson's disease-associated genes. Genetic testing revealed a c.988 C>T nonsense
133 mutation in the *IKBKG* gene, replacing glutamine at position 330 by a premature stop codon
134 (p.Gln330X) (Fig. 1B).

135 Based on our previous finding that NEMO is recruited to misfolded huntingtin with a
136 polyglutamine expansion (Htt-polyQ)³⁷, we wondered whether an *IKBKG* gene mutation
137 resulting in NEMO dysfunction is causally linked to neuronal protein aggregation observed in
138 our patient. A functional characterization of NEMO Q330X in cellular models showed that this
139 mutant is defective in NF- κ B signaling, explaining the clinical presentation with IP. In contrast
140 to wildtype (WT) NEMO, Q330X NEMO was not able to promote TNF-induced degradation of
141 I κ B α or NF- κ B transcriptional activity (Suppl. Fig. 1A-D). We observed impaired NF- κ B
142 activation by Q330X NEMO also upon IL-1 β receptor activation³⁸. However, our previous study
143 revealed that HOIP was able to decrease Htt-polyQ aggregates independently of NF- κ B
144 activation³⁷. Therefore, we wondered whether NEMO is a downstream effector of LUBAC-
145 mediated protein quality control. First, we tested if endogenous NEMO is recruited to protein
146 aggregates other than Htt-polyQ. Indeed, immunohistochemistry of brain slices from patients
147 with Parkinson's disease (PD), Alzheimer's disease (AD) or Frontotemporal dementia (FTD)
148 provided evidence for both NEMO and M1-linked ubiquitin chains colocalizing at aggregates
149 formed by α -synuclein, tau, or TDP-43 (Fig. 1C, D).

150

151 NEMO deficiency promotes protein aggregation under proteotoxic stress

152 To analyze a possible role of NEMO in proteostasis regulation, we quantified the amount of
153 protein aggregates induced by heat stress or proteasomal inhibition in wildtype and NEMO
154 knockout (KO) mouse embryonic fibroblasts (MEFs) by Proteostat[®], a red fluorescent
155 molecular rotor dye that binds to the cross-beta spine quaternary structure of aggregated

156 proteins. In the absence of NEMO, protein aggregation was significantly increased in response
157 to both heat stress and proteasome inhibition (Fig. 2A, B). In addition, NEMO-deficient cells
158 were more vulnerable to proteotoxic stress. Cell viability of NEMO KO MEFs was significantly
159 decreased in response to heat stress or proteasome inhibition compared to wildtype NEMO
160 MEFs (Suppl. Fig. 2A-C). We then made use of a luciferase-based sensor of proteostasis
161 capacity, the conformationally destabilized double mutant firefly luciferase FlucDM (R188Q,
162 R261Q) fused to EGFP^{39,40}. Imbalances in proteostasis induce misfolding and aggregation of
163 this sensor, which can be monitored by the formation of FlucDM-EGFP-positive foci and a
164 decrease in its luciferase activity. With the help of this sensor we compared the effects of
165 wildtype and Q330X NEMO under basal and proteotoxic stress conditions in a NEMO-deficient
166 background. NEMO KO MEFs transiently expressing FlucDM-EGFP and either wildtype or
167 Q330X NEMO were quantified for the abundance of EGFP-positive foci and for luciferase
168 activity. Heat stress (43°C, 20 min) increased FlucDM-EGFP foci formation and decreased its
169 luciferase activity in NEMO KO MEFs (Fig. 2C, D). Expression of wildtype NEMO significantly
170 reduced foci formation and increased luciferase activity of FlucDM-EGFP under both basal
171 and heat stress conditions, whereas Q330X NEMO had no effect (Fig. 2C, D). Interestingly,
172 NF- κ B was not activated by heat stress, as shown by an NF- κ B luciferase reporter assay and
173 a p65 nuclear translocation assay (Fig. 2E, F). In conclusion, NEMO plays a role in proteostasis
174 regulation that seems to be independent of NF- κ B activation.

175

176 **Misfolded α -synuclein is decorated with M1-linked ubiquitin and NEMO**

177 Since the NEMO-mutant patient showed a predominant α -synuclein pathology, we employed
178 cellular models of α -synuclein (aSyn) aggregation for mechanistic studies. Recombinant A53T
179 aSyn preformed fibrils (PFFs) were added as seeds to SH-SY5Y cells stably expressing A53T
180 aSyn fused to GFP (aSyn-GFP) to induce aggregation of aSyn-GFP^{41,42,43}. Intracellular aSyn
181 aggregates formed upon seeding showed characteristic features of pathologic aSyn, such as
182 phosphorylation at serine 129, insolubility in detergents, and non-dynamic behavior, as
183 determined by immunocytochemistry, immunoblotting and FRAP (fluorescence recovery after
184 photobleaching), respectively (Suppl. Fig. 3A-C). In addition, we characterized the aSyn seeds
185 by Thioflavin T fluorescence, dynamic light scattering, and liquid atomic force microscopy
186 (Suppl. Fig. 4A-F).

187 Consistent with our observation that M1-linked ubiquitin occurs at Lewy bodies in human brain
188 (Fig. 1C), linear ubiquitin chains co-localized with aSyn aggregates in SH-SY5Y cells after
189 seeding (Fig. 3A). Moreover, seeding of primary cortical neurons induced misfolding and serine
190 129 phosphorylation of endogenous aSyn, which stained positive for M1-linked ubiquitin (Fig.
191 3B). The presence of linear ubiquitin chains at aSyn in seeded SH-SY5Y cells was confirmed
192 biochemically by affinity purification of aSyn-GFP followed by immunoblotting using M1-

193 ubiquitin-specific antibodies ⁴⁴ (Fig. 3C). Moreover, endogenous NEMO was enriched at
194 seeded aSyn aggregates (Fig. 3D) and all three LUBAC components were recruited to aSyn
195 aggregates (Fig. 3E). In contrast, the RBR E3 ubiquitin ligase ARIH1 (ariadne homolog 1),
196 used as a control, was not recruited (Fig. 3E).

197

198 **The Q330X NEMO mutant does not bind to M1-linked ubiquitin chains and is not** 199 **ubiquitylated by HOIP**

200 To gain further insight into the function of NEMO in proteostasis regulation, we compared the
201 effect of wildtype NEMO and Q330X NEMO on aSyn aggregates in the SH-SY5Y seeding
202 model. We first tested for NEMO recruitment and observed that Q330X NEMO did not co-
203 localize with aSyn aggregates, whereas wildtype NEMO was strongly enriched at aSyn
204 aggregates (Fig. 4A). Defective recruitment of Q330X NEMO to protein aggregates was
205 confirmed in SH-SY5Y cells with Htt-polyQ aggregates, indicating that this phenomenon is not
206 limited to aSyn aggregates (Fig. 4B). We previously found that NEMO is recruited to Htt-polyQ
207 aggregates by binding to linear ubiquitin chains generated by HOIP (van Well, 2019). We
208 therefore compared the capacity of wildtype NEMO and Q330X NEMO to bind linear ubiquitin
209 chains. Lysates of cells expressing either wildtype or Q330X HA-tagged NEMO were incubated
210 with recombinant tetra-M1-ubiquitin (4xM1-ub), then NEMO was affinity-purified via its HA tag
211 and immunoblotted by using M1-ubiquitin-specific antibodies. In contrast to wildtype NEMO,
212 Q330X NEMO did not bind to tetra-M1-ubiquitin, although the UBAN domain (residues 296-
213 327) is not affected by the C-terminal deletion (Fig. 4C). Moreover, Q330X NEMO was not
214 modified by linear ubiquitin chains, although the key ubiquitin acceptor lysine residues (K285
215 and K309) are present in this mutant ⁴⁵. We induced M1-ubiquitination of HA-tagged NEMO by
216 either treating the cells with TNF or overexpressing the LUBAC components HOIP, HOIL-1L,
217 and SHARPIN (Fig. 4D). The cells were lysed under denaturing conditions, NEMO was
218 immunoprecipitated via its HA tag and analyzed by immunoblotting using M1-ubiquitin-specific
219 antibodies. Whereas wildtype NEMO was M1-ubiquitylated in both conditions, Q330X NEMO
220 was not even ubiquitylated upon the overexpression of LUBAC (Fig. 4D). Next, we analyzed
221 the interaction of wildtype NEMO and Q330X NEMO with endogenous HOIP by co-
222 immunoprecipitation experiments. The NZF1 domain of HOIP interacts with the coiled coil CC2
223 region upstream the UBAN domain of NEMO ^{45, 46, 47}. HOIP did not co-purify with Q330X
224 NEMO, which helps to explain why Q330X NEMO is not ubiquitylated (Fig. 4E).

225 Since NEMO not only binds to M1-linked polyubiquitin but also can be covalently modified by
226 HOIP, we followed up the hypothesis that NEMO increases M1-ubiquitylation at aSyn
227 aggregates. We generated NEMO KO SH-SY5Y cells by CRISPR/Cas9 and induced
228 aggregation of transiently expressed aSyn-GFP by adding aSyn seeds. NEMO KO SH-SY5Y
229 cells were reconstituted with either wildtype NEMO or Q330X NEMO and the colocalization of

230 M1-linked ubiquitin, NEMO and aSyn aggregates was quantified by the Pearson coefficient.
231 Colocalization of M1-linked ubiquitin and aSyn was strongly reduced when Q330X NEMO was
232 expressed in comparison to wildtype NEMO (Fig. 4F, G), suggesting that NEMO amplifies M1-
233 ubiquitylation at aSyn aggregates.

234

235 **A local NF- κ B signaling platform is assembled at aSyn aggregates which does not** 236 **promote a functional response**

237 It has been shown recently that LUBAC is recruited to intracellular bacteria, such as
238 *Salmonella enterica*, which can escape vacuoles and invade the cytosol^{48, 49, 50}. Modification
239 of the bacterial surface with linear ubiquitin chains by HOIP induces antibacterial autophagy
240 (xenophagy) and recruits NEMO for local activation of NF- κ B. We therefore tested whether an
241 NF- κ B signaling platform is also assembled at aSyn aggregates. Indeed, endogenous
242 phospho-IKK α / β (p-IKK α / β), p65, and phospho-65 (p-p65) were strongly enriched at aSyn
243 aggregates (Fig. 5A). However, we did not observe nuclear translocation of the NF- κ B subunit
244 p65 on day 1, 2, or 3 after seeding (Fig. 5B, C). To test whether NF- κ B signaling is
245 compromised in the presence of aSyn aggregates, we treated aSyn-expressing cells with TNF
246 on day 1, 2 and 3 after seeding. Whereas almost 100% of non-seeded cells showed nuclear
247 translocation of p65 in response to TNF treatment, p65 translocation was significantly reduced
248 upon seeding with only about 50% of cells positive for nuclear p65 on day 3 after seeding (Fig.
249 5B, C). Super-resolution structured illumination fluorescence microscopy (SR-SIM) revealed
250 that p65 is trapped at aSyn aggregates upon TNF stimulation, whereas in cells without aSyn
251 aggregates, TNF induced efficient nuclear translocation of p65 (Fig. 5C). Moreover, TNF-
252 induced nuclear translocation was also impaired in SH-SY5Y cells expressing Htt-Q97,
253 suggesting that pathogenic protein aggregates interfere with NF- κ B signaling (Fig. 5D). These
254 results indicated that although NF- κ B is locally activated at aggregates, functional NF- κ B
255 signaling is impaired most probably through sequestration of p65 and possibly other NF- κ B
256 pathway components at the aggregates.

257

258 **NEMO promotes autophagosomal degradation of α -synuclein in a p62-dependent** 259 **manner**

260 Our previous data indicated that NEMO is recruited to aSyn aggregates along with other NF-
261 κ B signaling components without inducing a functional NF- κ B response. Thus, NEMO seems
262 to have an NF- κ B-independent role in proteostasis regulation. Along this line, different protein
263 aggregates accumulate in the brain of the Q330X NEMO patient, and wildtype NEMO but not
264 Q330X NEMO reduces the fraction of cells with FlucDM-EGFP aggregates. LUBAC promotes
265 the autophagic clearance of cytosol-invading bacteria^{48, 49, 50}, we therefore wondered whether
266 linear ubiquitin chains can influence the degradation of protein aggregates by autophagy.

267 Intracellular aSyn can be degraded by both the proteasome and lysosomes depending on its
268 posttranslational modifications, conformational state and subcellular localization^{51, 52, 53}. To
269 test whether linear ubiquitylation promotes degradation of aSyn aggregates via autophagy, we
270 transiently expressed NEMO or HOIP in SH-SY5Y cells and quantified the fraction of cells with
271 aSyn aggregates 48 h after seeding. Both wildtype NEMO and wildtype HOIP, but neither
272 Q330X NEMO nor catalytically inactive C885A HOIP, decreased the number of cells with aSyn
273 aggregates (Fig. 6A, B). Notably, inhibition of lysosomal degradation by bafilomycin A1
274 abolished the ability of NEMO and HOIP to reduce the number of cells with aSyn aggregates
275 (Fig. 6A, B). We also tested the D311N NEMO mutant, which is defective in binding to M1-
276 linked ubiquitin^{54, 55}. Similarly to Q330X NEMO, D311N NEMO was impaired in modification
277 with M1- and K63-ubiquitin chains (Fig. S5A, B). Also, it was not recruited to aSyn aggregates
278 (Fig. S5A, B) and did not reduce aSyn aggregates (Fig. 6A).

279 Since NEMO and HOIP apparently promote the degradation of misfolded aSyn depending on
280 lysosomal function, we aimed at uncovering the underlying mechanism. Ubiquitylation is
281 decoded and translated into cellular effects by specific ubiquitin-binding proteins. We reasoned
282 that p62/SQSTM1 might be a promising candidate to test in our paradigm, based on its key
283 role in targeting protein aggregates for selective autophagy (aggrephagy)^{5, 56, 57, 58, 59}. The
284 ubiquitin-binding UBA domain of p62, which is required to shuttle cargo to the autophagic
285 machinery, binds to M1-linked ubiquitin with the strongest affinity compared to other ubiquitin
286 linkages⁶⁰. Moreover, p62 has been reported to interact with NEMO^{61, 62} and to co-localize
287 with Lewy bodies^{63, 64}. We confirmed that endogenous p62 binds to aSyn aggregates in our
288 seeding model (Fig. 6C) and that the recruitment of p62 to aSyn aggregates is dependent on
289 its UBA domain (Fig. S5C). Co-immunoprecipitation experiments using cell lysates revealed
290 that in contrast to wildtype NEMO, the Q330X NEMO mutant does not interact with
291 endogenous p62 (Fig. 6D).

292 To test for a role of p62 in mediating effects downstream of linear ubiquitylation, we analyzed
293 aSyn aggregates in p62-deficient MEFs (p62 KO MEFs) expressing aSyn-GFP. Two days after
294 seeding, about 75% of aSyn-GFP expressing p62 KO MEFs displayed aSyn aggregates.
295 Restoring p62 expression in p62 KO MEFs decreased the fraction of aggregate-positive cells
296 to about 55%, similarly to the extent of aSyn aggregation observed in wildtype SH-SY5Y cells.
297 Notably, the rescue effect of p62 was dependent on its UBA domain, since expression of p62-
298 ΔUBA had no effect on the number of cells with aSyn aggregates in p62 KO MEFs (Fig. 6E).
299 Increased expression of NEMO or HOIP in p62-deficient cells revealed a p62-dependent effect
300 of both NEMO and HOIP, seen after reconstituting p62 KO MEFs with wildtype p62 in
301 comparison to p62-ΔUBA (Fig. 6E). In addition, we observed a minor p62-independent effect
302 in reducing aSyn aggregates, most probably mediated by other ubiquitin-binding autophagy
303 receptors, such as NBR1. Notably, the p62-dependent effect of NEMO was blocked by

304 bafilomycin A1, confirming that p62 decreased aSyn aggregates downstream of NEMO by
305 autophagosomal clearance (Fig. 6F).

306 Next, we wondered whether defective p62-dependent autophagosomal degradation of aSyn
307 might explain the accumulation of aSyn aggregates in the Q330X NEMO patient. We analyzed
308 brain sections from the Q330X NEMO patient by immunohistochemistry and found that
309 colocalization of p62 with aSyn-positive aggregates was significantly reduced in comparison
310 to patients suffering from other α -synucleinopathies, such as Dementia with Lewy Bodies
311 (DLB) (Fig. 7A, B). Of note, p62 signal intensity was strongly increased in the Q330X NEMO
312 patient's brain, possibly reflecting a compensatory up-regulation of p62 expression (Fig. 7C).
313 Encouraged by these findings, we wondered whether the NEMO-dependent recruitment of p62
314 to aSyn aggregates can also be seen in cellular models. We induced aggregation of transiently
315 expressed aSyn-GFP in NEMO KO SH-SY5Y cells by adding aSyn seeds. Colocalization of
316 endogenous p62 and aSyn aggregates was quantified by the Pearson coefficient, which
317 revealed a significant decrease in NEMO KO cells compared to control cells (Fig. 7D, E). In
318 conclusion, our data from human brain samples and cellular models indicated that NEMO
319 deficiency impairs the recruitment of the selective autophagy adaptor protein p62 to aSyn
320 aggregates.

321

322 **NEMO promotes p62 condensate formation at aggregates by lowering the threshold for** 323 **ubiquitin-induced phase transition**

324 When analyzing p62 recruitment to aSyn aggregates in NEMO-deficient cells by SR-SIM, we
325 noticed a different pattern of p62 localization at aggregates. Whereas p62 mostly formed foci
326 at the aggregate surface in the presence of NEMO, it showed a more uniform distribution
327 around the aggregates in the absence of NEMO (Fig. 7D, Fig. 8A, B). Notably, ubiquitin-
328 dependent p62 condensation is required for efficient autophagic clearance of cargo^{65, 66, 67, 68,}
329⁶⁹. We and others recently observed that NEMO undergoes phase separation upon binding to
330 linear ubiquitin chains⁷⁰. Since Q330X NEMO is impaired in binding to M1-linked ubiquitin, it
331 does neither phase-separate *in vitro* nor form condensates in cells³⁸. We therefore speculated
332 that NEMO by interacting with M1-linked ubiquitin chains at protein aggregates may prime the
333 aggregate surface for efficient p62 condensate formation. Fluorescence recovery after
334 photobleaching (FRAP) of Halo-tagged NEMO expressed in NEMO-KO cells indicated that
335 NEMO forms a mobile phase at aSyn aggregates (Fig. 8C). We also observed by SR-SIM
336 microscopy that endogenous p62, NEMO and M1-linked ubiquitin colocalize in condensates
337 at aSyn aggregates (Fig. 8D). This observation prompted us to study a possible effect of
338 NEMO on ubiquitin-induced p62 condensation *in vitro*. We first tested whether p62 and NEMO
339 can co-condensate. Recombinant mCherry-p62 and NEMO-GFP were mixed with or without
340 recombinant tetra- or octa-M1-linked ubiquitin. Laser scanning microscopy revealed that co-

341 condensation of p62 and NEMO occurred only in presence of tetra- or octa-M1-linked ubiquitin,
342 but not in the absence of M1-linked ubiquitin (Fig. 8E). We then studied p62 condensate
343 formation dependent on the concentration of p62 and tetra- or octa-M1-linked ubiquitin (from
344 0.5 to 10 μ M each) in the presence and absence of NEMO. As illustrated by phase diagrams,
345 NEMO shifted p62 phase transition to the lowest concentration of both p62 and tetra- or octa-
346 M1-ubiquitin (Fig. 8F). Thus, by co-condensation with p62 and M1-linked ubiquitin, NEMO
347 facilitates the local concentration of p62. These results provide a mechanistic explanation for
348 the impaired autophagic clearance of protein aggregates in the absence of functional NEMO
349 observed in our cellular models and the Q330X NEMO patient brain samples.

350

351 **DISCUSSION**

352 Here we demonstrate that NEMO has an NF- κ B-independent role in maintaining cellular
353 proteostasis. NEMO-deficient cells accumulate misfolded proteins upon proteotoxic stress and
354 are hypersensitive to proteostasis dysregulation. The crucial role of NEMO in maintaining
355 proteostasis is confirmed by the neuropathological alterations found in the Q330X NEMO-
356 mutant patient, who shows a progressive widespread mixed brain proteinopathy with
357 predominant aSyn pathology. Studying this NEMO mutant revealed that LUBAC-mediated
358 formation of linear ubiquitin chains and binding of NEMO to linear ubiquitin chains are required
359 to promote autophagosomal degradation of misfolded aSyn through the selective autophagy
360 receptor p62. We previously reported that wildtype NEMO in contrast to Q330X NEMO has
361 the propensity to form phase-separated condensates upon binding to linear ubiquitin chains
362 ³⁸. Here we show that through this propensity NEMO facilitates p62-dependent autophagy.
363 Condensate formation with ubiquitinated cargo is a crucial event in p62-mediated autophagy,
364 since it contributes to the recruitment of the autophagic machinery ^{65, 66, 67, 68, 69}. Whereas the
365 mechanism of autophagy initiation by p62 has been studied in great detail, little is known about
366 processes at the aggregate interface required to locally concentrate and rearrange p62. Our
367 study identified NEMO as a major player in priming the aggregate interphase for p62
368 condensation. At least two NEMO-dependent processes seem to be relevant in this context.
369 First, NEMO amplifies linear ubiquitination at protein aggregates. This is accomplished by both
370 binding to M1-linked ubiquitin and its M1-ubiquitylation by HOIP. HOIP is recruited to protein
371 aggregates by VCP/p97 and can generate free, unanchored M1-linked polyubiquitin ³⁷,
372 suggesting that the aggregated protein not necessarily needs to be covalently modified by
373 HOIP, since NEMO would be an available substrate. Accordingly, we found M1-linked ubiquitin
374 and NEMO at various protein aggregates, including aSyn, Htt-polyQ, tau, and TDP-43.
375 Second, binding of NEMO to M1-linked ubiquitin generates a mobile phase-separated
376 aggregate surface, facilitating the local concentration of p62 by co-condensation. Indeed,

377 liquidity at the cargo surface seems to be an important prerequisite for efficient selective
378 autophagy^{71, 72, 73, 74, 75}.

379 LUBAC-mediated quality control of cellular protein aggregates shares some similarities with
380 its role in anti-bacterial autophagy. Bacteria that escape from the vacuolar compartment into
381 the cytosol, such as *Salmonella* species, are coated by ubiquitin to restrict bacterial
382 proliferation^{48, 49, 50}. In this pathway, the RNF213 ubiquitin ligase ubiquitylates the bacterial
383 outer membrane component lipopolysaccharide (LPS), which is a prerequisite for the
384 subsequent recruitment of LUBAC⁵⁰. HOIP binds to pre-existing ubiquitin at the bacterial
385 surface and assembles M1-linked ubiquitin chains on bacterial membrane proteins or on
386 ubiquitin moieties previously attached by RNF213. Linear ubiquitin chains then recruit
387 Optineurin and NEMO to the bacterial surface, which both bind to M1-linked ubiquitin with high
388 affinity via their UBAN domain. Whereas Optineurin induces selective autophagy to promote
389 the clearance of bacteria, NEMO locally activates the IKK complex and thereby transforms the
390 bacterial surface into an NF- κ B signaling platform^{48, 49}. LUBAC-mediated aggrephagy differs
391 from bacterial xenophagy in some substantial aspects. First, HOIP is recruited to cytosolic
392 bacteria via its NZF domain by pre-existing ubiquitin assembled by RNF213⁵⁰, whereas
393 VCP/p97 is required to recruit HOIP to misfolded proteins by an interaction of the PIM domain
394 of VCP/p97 with the PUB domain of HOIP³⁷. Second, Optineurin is required for antibacterial
395 autophagy, whereas for the clearance of misfolded aSyn p62 plays a major role, though we
396 cannot exclude an additional role of Optineurin. Third, NEMO is apparently dispensable for
397 bacterial autophagy⁴⁸ but required for autophagic degradation of aSyn. This difference may
398 be attributable to the fact that p62 is a key cargo receptor in aggrephagy. The increased
399 abundance of p62 in the brain of the Q330X NEMO patient may reflect either a compensatory
400 upregulation by transcription factors other than NF- κ B, such as NRF2⁷⁶, or an accumulation
401 of p62 due to a decreased autophagic flux. Interestingly, the *Drosophila melanogaster* NEMO
402 homolog Kenny has a LIR motif that interacts with Atg8/LC3 and promotes the autophagic
403 degradation of the IKK complex in order to prevent constitutive production of antimicrobial
404 peptides against commensal microbiota⁷⁷. According to a mathematical model proposed by
405 Tusco et al., host-pathogen co-evolution could have been the driving force for the loss of the
406 LIR motif in mammalian NEMO⁷⁷.

407 Even though the role of LUBAC and NEMO in protein quality control seems to be independent
408 of NF- κ B signaling, impaired activation of the NF- κ B prosurvival pathway may contribute to the
409 toxicity of protein aggregates. Whereas prolonged and excess NF- κ B activation is associated
410 with inflammation, constitutive NF- κ B signaling in neurons regulates synaptic plasticity and
411 neuronal viability^{78, 79, 80, 81, 82}. Moreover, induced NF- κ B activation protects from neuronal cell
412 death in various stress conditions^{82, 83, 84, 85}. Of note, several neurotrophic proteins, such as
413 NGF, BDNF and GDNF, signal via NF- κ B to promote neuronal viability^{86, 87, 88, 89, 90}. Our data

414 indicate that similarly to intracellular bacteria, an NF- κ B signaling platform is assembled at
415 aSyn aggregates. However, this signaling platform is not functional, since p65 seems to be
416 sequestered and trapped at the aggregates so that not even an additional NF- κ B-activating
417 stimulus, like TNF, promotes nuclear translocation of p65. Thus, prosurvival signals cannot
418 efficiently be transduced via NF- κ B in cells with aSyn or Htt-polyQ aggregates. It is noteworthy
419 in this context that our study revisits an earlier finding linking NEMO to Parkinson's disease.
420 We previously discovered that linear ubiquitination of NEMO is a prerequisite for Parkin to
421 prevent stress-induced neuronal cell death. This activity of Parkin was associated with adding
422 K63-linked ubiquitin to NEMO, suggesting that Parkin can act as a priming E3 ligase for
423 subsequent modification of NEMO by LUBAC^{91,92}. Whether Parkin also plays a role in LUBAC-
424 mediated protein quality control is an interesting question to be addressed in further studies.
425 Finally, our study adds to the notion that different neurodegenerative diseases share common
426 pathways. The accumulation of various proteins linked to neurodegeneration in the brain of
427 the Q330X NEMO patient reflects a general neuronal proteostasis dysregulation, which at least
428 partially can be explained by defective p62-mediated selective autophagy. The presence of α -
429 synuclein, tau and TDP-43 aggregates has also been reported in some patients with *OPTN*
430 mutations affecting the UBAN domain of Optineurin, which binds linear ubiquitin chains⁹³.
431 Thus, neurodegeneration in these patients may also be linked to defective protein quality
432 control downstream of LUBAC. Shared pathomechanisms related to proteostasis
433 dysregulation may entail specific targets for disease-modifying strategies. Further studies need
434 to address whether the linear ubiquitination machinery can be exploited for therapeutic
435 approaches.

436

437 **MATERIALS AND METHODS**

438 **DNA constructs**

439 The following constructs were described previously: human HOIP, HOIL-1L, SHARPIN, HA-
440 HOIP, HOIL 1L-HA, SHARPIN-HA, HA-HHARI, FLAG-NEMO wt, FLAG-NEMO D311N, HA-
441 IKK β , mCherry, NF- κ B-luciferase reporter⁹¹; HA-HOIP C885A, Htt-Q25-GFP, Htt-Q97-GFP³⁷;
442 p62 and p62 Δ UBA⁵⁷. HA-NEMO wt and HA-NEMO D311N were generated using the following
443 primers: HA-NEMO-fwd: 5'-ATATGGATCC AATAGGCACCTCTGGAAGAGC-3', HA-NEMO-
444 rev: 5'-ATATGCGGCCGC CTAATCAATGCACTCCATGACATG-3' The amplified fragment
445 was digested with BamHI and NotI and cloned into pcDNA3.1-N-HA. HA-NEMO Q330X was
446 generated using the following primers: HA-NEMO Q330X-fwd: 5'- ATAT GGATCC
447 AATAGGCACCTCTGGAAGAGC-3', HA-NEMO Q330X-rev: 5'-
448 ATATGCGGCCGCTCACAGGAGCTCCTTCTTCTCGG-3'. The amplified fragment was
449 digested with BamHI and NotI and cloned into pcDNA3.1-N-HA. FLAG-NEMO Q330X was
450 generated using the following primers: FLAG-NEMO Q330X-fwd 5'- GCGC AAGCTT

451 ATGGACTACAAGGATGATGATGACAAG-3', FLAG-NEMO Q330X-rev 5'- ATAT TCTAGA
452 CTACAGGAGCTCCTTCTTCTCGGC-3' The amplified fragment was digested with HindIII and
453 XbaI and cloned into pEF4 -N-FLAG. HA-IkBa was generated using the following primers: HA-
454 IkBa-fwd: 5'- ATAT GGATCC ACCGAGGACGGGGACTCG-3', HA-IkBa-rev: 5'- ATAT
455 GCGGCCGC CTATAACGTCAGACGCTGGCC-3' The amplified fragment was digested with
456 BamHI and NotI and cloned into pcDNA3.1-N-HA. p62ΔUBA-HA (AA 1-388) was generated
457 using the following primers: p62ΔUBA-HA-fwd: 5'- ATAT GAATTC GCCACC ATG GCG TCG
458 CTC ACC GTG-3', p62ΔUBA-HA-rev 5'- TATAGCGGCCGC T GGC GGG AGA TGT GGG
459 TAC-3' The amplified fragment was digested with EcoRI and NotI and cloned into pcDNA3.1-
460 C-HA. aSyn A53T-GFP was generated using the following primers: α-Synuclein A53T-eGFP-
461 fwd: 5'- ATAT AAGCTT GCCACC ATG GAT GTA TTC ATG AAA GGA C-3', α-Synuclein
462 A53T-eGFP-rev: 5'- ATATGCGGCCGC GCGCTTCAGGTTCTAGTC-3' The amplified
463 fragment was digested with HindIII and NotI and cloned into pcDNA3.1-C-eGFP.

464

465 **Cell lines**

466 HEK293T cells (CRL-1573; American Type Culture Collection) were cultured in Dulbecco's
467 modified Eagle's medium (DMEM) supplemented with 10% (v/v) fetal bovine serum (FBS) and
468 100 IU/ml penicillin 100 µg/ml streptomycin sulfate. SH-SY5Y (DSMZ number ACC 209), were
469 cultured in Dulbecco's modified Eagle's medium F-12 (DMEM/F12) supplemented with 15%
470 (v/v) fetal bovine serum (FBS), 100 IU/ml penicillin 100 µg/ml streptomycin sulfate and 1%
471 non-essential amino acids. Mouse embryonic fibroblasts (MEFs) derived from wild-type or
472 NEMO KO mice⁹⁴ or p62 KO mice⁹⁵ were cultured in Dulbecco's modified Eagle's medium
473 (DMEM) supplemented with 10% (v/v) fetal bovine serum (FBS) and 100 IU/ml penicillin 100
474 µg/ml streptomycin sulfate.

475

476 **Generation of NEMO CRISPR/Cas9 knockout (KO) SH-SY5Y cells and HOIP** 477 **CRISPR/Cas9 KO HeLa cells**

478 sgRNAs (RNF31-24147982 AGGGUGUUGAGGUAGUUUCG; RNF31-24147993
479 GAGCCGUGGACAGGGUGUUG; IKBKG-154552050 UGUGAGAUGGUGCAGCCCAG;
480 IKBKG-154552185 GAGGAGAAUCAAGAGCUCCG) were designed using the Synthego
481 website (www.design.synthego.com). 1.5 nmol sgRNAs were rehydrated in 50 µl nuclease-
482 free 1 x TE buffer (10 mM Tris-HCl, 1 mM EDTA, pH 8.0) to a final concentration of 30 µM (30
483 pmol/µl). sgRNA and recombinant CAS9 were delivered as ribonucleoprotein (RNP)
484 complexes using a 4D-Nucleofector X-Unit (Lonza). Briefly, for the assembly of the RNP
485 complexes, Cas9 2NLS and sgRNAs were combined in Nucleofector™ solution at a molar
486 ratio of 9:1 sgRNA to Cas9 and incubated for 10 min at room temperature. The cells were
487 resuspended at a concentration of 150,000 cells/5 µl. 5 µl of the cell suspension was added to

488 the 25 μ l of pre-complexed RNPs for a total transfection volume of 30 μ l per reaction and
489 transferred to Nucleofector cartridges. Nucleofection was performed according to the
490 predefined protocol (CA-137 for SH-SY5Y- and CN-114 for HeLa cells) and cells were carefully
491 resuspended in each well of the Nucleocuvette™ with 70 μ l of pre-warmed growth medium
492 and transferred to the pre-warmed 6-well and incubated in a humidified 37°C/5% CO₂
493 incubator. After 24 h the medium was replaced.

494 For clone screening, the cells were split into two 6-well cell culture plates, and pools were
495 analyzed by PCR and subsequent DNA sequencing. For this, primer pairs (HOIP_fwd:
496 AGTCCCACCCTCTCTCCTAG, HOIP_rev: TGTGACTGTAGCAACCTGGT, NEMO_fwd:
497 CCTGGAGCTAGGCCTTTTCA, NEMO_rev: ACTTCCTCCCGCTAATCTG) were ordered
498 extending approx. 200-250 bp 3' and 5' of the sgRNA binding region. To perform cell pool or
499 single clone sequencing analysis, genomic DNA was isolated using a genomic DNA extraction
500 kit (Monarch Genomic DNA Purification Kit, New England Biolabs, Frankfurt am Main,
501 Germany) and the PCR was optimized to yield a single amplicon. Following PCR product
502 purification (NucleoSpin Gel and PCR Clean-up, Macherey-Nagel GmbH, Düren, Germany),
503 the DNA was sent for Sanger sequence analysis (Microsynth Seqlab GmbH, Göttingen,
504 Germany). The KO efficiency of the cell pools and single colony clones was determined using
505 the SYNTHOGO ICE analysis website (<https://ice.synthego.com>). To isolate single KO clones,
506 the KO cell pools were diluted to 1 cell/100 μ l and 5 cells/100 μ l and the dilutions were
507 distributed over several 96-well plates. 15-25 clones were grown from single cells and
508 reanalyzed using the above-mentioned process. Finally, clones with a high KO score were
509 amplified and KO efficiency was confirmed by immunoblotting.

510

511 **Recombinant expression and purification of recombinant proteins**

512 Recombinant α -synuclein expression and seeding was performed as described previously ⁴².
513 ⁴³. Briefly, α -synuclein (aSyn) A53T encoded on a pT7-7 plasmid was transformed into *E. coli*
514 strain BL21 (DE3). Bacteria were grown in Terrific Broth medium supplemented with ampicillin
515 at 37°C to a density of an A600 value of 0.8-1.0, and protein expression was induced by adding
516 1 mM IPTG for 4 h at 37°C. Bacteria were harvested by centrifugation (6000 rcf, 20 min, 4 °C).
517 Pellet was resuspended in high-salt buffer (750 mM NaCl, 10 mM Tris, pH 7.6, 1 mM EDTA,
518 protease inhibitor tablet (Roche)) and lysed by sonication at 60% power using a probe
519 sonicator (Branson sonifier 450) for a total time of 5 min (30 s pulse on, 30 s pulse off), followed
520 by boiling of the sample for 15 min. After cooling on ice, the sample was centrifuged for 20 min
521 at 6000 rcf. The supernatant was dialyzed overnight with 10 mM Tris, pH 7.6, 50 mM NaCl, 1
522 mM EDTA. Protein was concentrated with a 3.5 kDa MWCO Amicon ultracentrifuge filter
523 device (Millipore). After filtering the protein through a syringe filter (0.45 μ m), the soluble
524 proteins were separated by size exclusion chromatography on a Superdex 200 column (GE

525 Healthcare Life Sciences). 40 2 ml fractions were collected using an ÄKTA chromatography
526 system (GE Healthcare Life Sciences). Collected fractions were analyzed by SDS-PAGE using
527 a 16% (w/v) polyacrylamide-gel followed by Coomassie staining/destaining. Fractions
528 containing aSyn A53T were combined and dialyzed over night with 10 mM Tris, pH 7.6, 25 mM
529 NaCl, 1 mM EDTA. On the next day, the combined fractions were subjected to anion-exchange
530 chromatography on two connected 5 ml HiTrap Capto Q ImpRes (GE Healthcare Life
531 Sciences) anion-exchange columns using a linear gradient, ranging from 25 mM NaCl to 1 M
532 NaCl. Forty 2 ml fractions were collected using an ÄKTA chromatography system (GE
533 Healthcare Life Sciences). Collected fractions were analyzed by SDS-PAGE using a 16% (w/v)
534 polyacrylamide-gel followed by Coomassie staining/destaining. Fractions containing aSyn
535 A53T were combined and dialyzed over night with 50 mM Tris, pH 7.5, 150 mM KCl. Protein
536 was concentrated with a 3.5 kDa MWCO Amicon ultracentrifuge filter device (Millipore) to a
537 concentration of 5 mg/ml. Aliquots of 1 ml were stored at -80 °C.

538 To prepare recombinant seeds for the induction of aSyn aggregates in SH-SY5Y cells stably
539 expressing aSyn A53T-GFP, an aliquot containing 1 ml aSyn A53T with a concentration of 5
540 mg/ml was thawed on ice and centrifuged (20,000 rcf, 30 min, 4°C). The supernatant was
541 transferred into a new tube and incubated on a thermomixer for 24 h at 37°C, 900 rpm. The
542 sample was divided into 50 µl aliquots and stored at -80°C until further use.

543 pET-Duet1-6xHis-mCherry-p62⁶⁰ was recombinantly expressed and purified from *E. coli*
544 Rossetta (DE3) pLysS cells. Bacteria were grown in Luria broth (LB) medium until OD600 ≈
545 0.6, then induced with 0.3mM isopropylthiogalactoside (IPTG) and grown at 20°C for overnight.
546 Harvested cells were resuspended in lysis buffer 50 mM 4-(2-hydroxyethyl)-1-
547 piperazineethanesulfonic acid (HEPES) at pH 7.5, 500 mM NaCl, 10 mM imidazole, 2 mM
548 MgCl₂, 2 mM β-mercaptoethanol, complete protease inhibitor and DNase I and lysed by French
549 press. Lysates were cleared by ultracentrifugation at 40,000 g for 45 min at 4°C. Supernatants
550 were applied to Nickel-Nitrilotriacetic (Ni-NTA) His-Trap FF column (GE Healthcare) and
551 6xHis-tagged-mCherry-p62 was eluted via a stepwise imidazole gradient (50, 75, 100, 150,
552 200, and 300 mM). Protein-containing fractions were pooled and dialysed overnight at 4°C in
553 storage buffer containing 50 mM HEPES pH 7.5, 500 mM NaCl, 2 mM MgCl₂, 2 mM β-
554 mercaptoethanol. The protein was filtered using a 0.45 µm syringe, aliquoted and flash frozen
555 until further use.

556 Wildtpye NEMO-GFP and 4xM1-ubiquitin were expressed and purified as described previously
557 ³⁸.

558 8xM1-ub was commercially bought from Enzo Life Sciences.

559

560 **Induction of α-Synuclein aggregates by α-Synuclein A53T seeds in cultured cells and**
561 **primary neurons**

562 SH-SY5Y cells stably expressing aSyn A53T-GFP or MEFs transiently expressing aSyn-
563 A53T-GFP were cultivated on glass coverslips (Laboratory Glassware Marienfeld) for
564 immunofluorescence analysis or on cell culture dishes for biochemical analysis. 24 h after
565 plating, transient transfection, or gene silencing, freshly sonicated aSyn A53T seeds were
566 added to the cells to a final concentration of 12.5 µg/ml as follows:

567 50 µl of aSyn A53T seeds were thawed at room temperature and added to 950 µl Opti-MEM
568 (Gibco) to obtain a concentration of 250 µg/ml. Sonication was performed with a probe
569 sonicator (Branson sonifier 450) for 3 min (30 % power, 10 s intervals). Sonicated seeds were
570 added to 960 µl of Opti-MEM plus 40 µl Lipofectamine 2000 (Invitrogen) in order to increase
571 uptake of seeds by the cells, to a final concentration of 125 µg/ml. After incubation for 15 min
572 at room temperature, the seed solution was added to cells to obtain a final concentration of
573 12.5 µg/ml per well in Opti-MEM. After 24 h the cells were either harvested, fixed for
574 immunofluorescence experiments, or Opti-MEM was exchanged by Dulbecco's modified
575 Eagle's medium F-12 (DMEM/F12) supplemented with 15% (v/v) FCS, 1% (v/v)
576 Penicillin/Streptomycin (Gibco) and 1% (v/v) minimum essential medium non-essential amino
577 acids (Gibco), and cells were further grown for 24 to 48 h prior to harvesting or fixing.

578 For the induction of aSyn aggregation in primary cortical mouse neurons by aSyn A53T seeds,
579 cells were plated on poly-L-lysine- and laminin-coated coverslips, and sonicated aSyn A53T
580 seeds were added on DIV 5 to a final concentration of 1 µg/ml. Primary neurons were fixed
581 with 4 % PFA 7 days after seeding and prepared for immunocytochemistry.

582

583 **Detergent solubility assay**

584 SH-SY5Y cells stably expressing aSyn A53T-GFP were grown in 3.5 cm dishes and harvested
585 in cold PBS 24, 48, or 72 h after seeding with aSyn A53T seeds. Cells were lysed 10 min on
586 ice in 1% (v/v) Triton X-100 in TBS supplemented with protease inhibitor (cOmplete, Roche)
587 and phosphatase inhibitor (PhosStop, Roche). Samples were centrifuged (15 min, 20,000 rcf,
588 4°C), the supernatants were transferred into new tubes, and 5x Laemmli sample buffer was
589 added (1 % Triton X-100-soluble fraction). The pellets were washed two times with lysis buffer,
590 solved in 1% (w/v) SDS in TBS, and boiled 15 min at 99°C. In addition, DNA was sheared by
591 passing the samples 15 times through a 23-Gauge needle. Finally, 5x Laemmli sample buffer
592 was added (1% SDS-soluble fraction). Equal amounts of the two fractions were used for
593 analysis by immunoblotting using the indicated antibodies.

594

595 **Immunocytochemistry**

596 Cells were cultivated on glass coverslips (Laboratory Glassware Marienfeld). For some
597 experiments, coverslips were coated with both poly-L-lysine (PLL) (Sigma) and laminin
598 (Sigma) or PLL only. 24–72 h after seeding with aSyn A53T seeds, the cells were fixed for 10

599 min with 4% paraformaldehyde in PBS or Tris pH 7.4, and permeabilized and blocked in 0.2%
600 (v/v) Triton X-100, 5% (v/v) goat serum in PBS or Tris for 2 h. Cells were stained with primary
601 antibodies at a dilution of 1:100 to 1:1000 in 0.2% (v/v) Triton X-100, 5% (v/v) goat serum in
602 PBS or Tris at 4°C overnight, washed 3x with PBS or Tris, and incubated with fluorescent dye-
603 conjugated secondary antibodies Alexa Fluor 488, 555, or 647 (Thermo Scientific), at a dilution
604 of 1:1000 for 1 h at room temperature. After extensive washing, cells were mounted in
605 Fluoroshield G (Thermo Scientific) with DAPI (Sigma).

606

607 **Human brain sections**

608 *Post mortem* brain samples from the Q330X NEMO patient, from DLBD patients and from
609 respective controls were provided by the Department of Pathology, University of California,
610 San Francisco, California, USA. PD brain samples were provided by the Charité
611 Universitätsmedizin Berlin, Germany. *Post mortem* brain samples of frontal isocortex from
612 neuropathologically confirmed AD, DLBD, FTLD and tauopathy patients were obtained from
613 the Institute of Neuropathology, University Medical Center Hamburg-Eppendorf, Hamburg,
614 Germany. Ethical review for the use of anonymized human post-mortem tissues was
615 performed according to the guidelines of the local ethical committees. Available data are
616 listed in the supplementary Table1.

617

618 **Immunohistochemistry**

619 For peroxidase immunohistochemistry, paraffin-embedded brain sections (5 µm) were
620 deparaffinized with xylene and ethanol and briefly washed with deionized water. Brain sections
621 were cut from archived paraffin tissue blocks obtained during routine brain autopsy after whole-
622 brain fixation in formalin for at least two weeks. Antigen retrieval through microwaving in 100
623 mM citrate buffer pH 6.0 was followed by blocking of endogenous peroxidase with 5% H₂O₂ in
624 methanol. Then sections were transferred in PBS with 0.02% Brij35 and blocked with 2% FBS
625 in PBS. Incubation with the primary antibody was performed overnight at 4°C. After rinsing with
626 0.02 % Brij35 in PBS, antibody binding was detected and enhanced by DCS Super Vision 2
627 HRP-Polymer-Kit (DCS, Germany) using the chromogen DAB. Counterstaining with
628 hematoxylin for cellular structures was performed. Microscopic images were obtained with a
629 BX50 microscope and Cell-D software (Olympus).

630 For immunofluorescence histochemistry, paraffin-embedded human brain sections were
631 deparaffinized and antigen retrieval was performed as described above. Sections were
632 blocked and permeabilized with 10% (v/v) goat serum, 0.3% (v/v) Triton X-100 in PBS for 1 h.
633 Primary antibodies at a dilution of 1:50 (α-synuclein), 1:100 (Tau, TDP-43, M1Ubi and NEMO)
634 or 1:250 (p62) in 10% (v/v) goat serum, 0.3% (v/v) Triton X-100 in PBS were incubated at 4°C
635 for 48 h. After the brain sections were washed 3x with PBS and blocked with 2% (w/v) BSA in

636 PBS for 1 h, they were incubated with fluorescent dye-conjugated secondary antibodies Alexa
637 Fluor 488 and 555 (Thermo Scientific) at a dilution of 1:1000 in 2% (w/v) BSA in PBS at room
638 temperature for 1 h. After extensive washing, sections were mounted with Prolong Gold
639 including DAPI (Thermo Fisher Scientific). Confocal images were obtained using a Zeiss
640 ELYRA PS.1 equipped with an LSM880 (Carl Zeiss, Oberkochen). Super-resolution and
641 confocal images were processed using the ZEN2.1 software (Carl Zeiss, Oberkochen).

642

643 **Fluorescence Microscopy**

644 Fluorescence microscopy was performed using a Zeiss ELYRA PS.1 system equipped with an
645 LSM880 (Carl Zeiss, Oberkochen) and a 20x/0.8, 63x/1.4 oil or 100x/1.46 oil immersion
646 objective or a C2+ system (Nikon). Super-resolution images were generated by the Structured
647 Illumination (SIM) technology using 405, 488, 561 and 647 nm widefield laser illumination. SIM
648 confocal images were processed using the ZEN Black software (Carl Zeiss, Oberkochen),
649 image data were exported using the ZEN Blue software for further use. For the analysis of
650 stained human brain sections, laser scanning microscopy was performed using the 405, 488,
651 561 and 647 nm laser illumination set in individual channels to avoid cross-talk. The pinhole
652 was adjusted to generate optical section of 2-5 μm , the acquisition settings were kept constant
653 throughout the experiment. For the analysis of p62 positive aSyn aggregates in human brain
654 sections, a 2x2 tile scan using the 20x/0.8 objective acquired and subsequently stitched with
655 ZEN Black software.

656 *Colocalization studies*

657 To investigate the colocalization of aSyn, NEMO and M1-ub, the respective cell lines were
658 transiently transfected with pcDNA3.1 aSyn A53T-GFP and seeded with aSyn seeds as
659 described above. After 48 h the cells were fixed and stained with the respective antibodies as
660 described in under Immunocytochemistry. To quantify the colocalization of NEMO and aSyn,
661 M1-ub and NEMO, and M1-ub and aSyn, samples were imaged with constant laser settings
662 and respective signal thresholds were set to specific signal intensities and kept constant
663 throughout the experiment. A contour was drawn around each protein aggregate and the
664 Pearson colocalization coefficient within the contour was plotted for each comparison.

665 *Analysis of condensate formation*

666 Fluorescent imaging laser scanning microscopy was performed using an LSM880 (Carl Zeiss,
667 Oberkochen) with a 63 \times oil immersion objective. A 63 \times NA 1.4 oil immersion objective was
668 used to record a z-stack of 67.5 \times 67.5 \times 10 and 0.330 μm for each optical section. The argon
669 laser power was set to 0.006% at 488 nm with pixel dwell time of 5.71 μs . During all
670 measurements, laser power, gain, and field of view were kept constant. The Z-stacks were
671 then processed to obtain maximum intensity projections.

672

673 **Immunoprecipitations**

674 Cells were lysed in 1% (v/v) Triton X-100 in PBS supplemented with 30 mM NEM (Sigma),
675 protease inhibitor (cOmplete, Roche) and phosphatase inhibitor (PhosStop, Roche). The
676 lysates were cleared by centrifugation (20,000 × g, 4°C, 15 min). Samples were incubated
677 overnight with anti-HA magnetic beads (Thermo Scientific) or for 5 h with GFP-Trap magnetic
678 agarose (Chromotek) at 4°C under rotation. Beads were washed five times with 1% (v/v) Triton
679 X-100 in PBS. Immunopurified proteins were eluted by adding 2x Laemmli sample buffer and
680 boiling for 10 min at 95°C. Samples were analyzed by immunoblotting using the indicated
681 antibodies.

682

683 **P65 translocation assay**

684 SH-SY5Y cells stably expressing α -Synuclein A53T-GFP were plated on cover slips, and after
685 24h they were treated with α -Synuclein A53T seeds (+ seeds) or PBS as a control (- seeds).
686 One, two, and three days post-seeding, cells were treated with 25 ng/ml TNF (PeproTech) for
687 15 min as indicated and fixed with PFA. Samples were analyzed by immunocytochemistry
688 using an antibody for p65. Nuclear translocation was quantified using the green, red, and DAPI
689 channel of a fluorescence microscope (Nikon Eclipse E400).

690

691 **Quantification of aSyn A53T-GFP aggregates**

692 After preparation of the samples on coverslips, they were analyzed using the green, red, and
693 DAPI channel of a fluorescence microscope (Nikon Eclipse E400). Cells containing aggregates
694 or fibrillar structures of aSyn A53T-GFP were counted positive, cells with neither aggregates
695 nor fibrillar structures but with cytosolic and nuclear GFP staining were counted negative.
696 When plasmids were transiently transfected during sample preparation, only cells positive for
697 the transfected construct were considered. For quantification of the percentage of cells with
698 aggregates five independent experiments were performed, and at least 150 cells were
699 analyzed per condition for each replicate.

700

701 **Sedimentation assay**

702 An aliquot of both aSyn A53T seeds and aSyn A53T monomers was thawed at room
703 temperature. 10 μ l of each sample was centrifuged for 10 min at 20,000 rcf, respectively. The
704 supernatant was transferred into a new tube and 10 μ l of 2x Laemmli sample buffer was added
705 (sup). The pellets were resuspended in 200 μ l PBS and centrifuged again (20,000 rcf, 10 min).
706 Supernatants were discarded and 10 μ l PBS and 10 μ l 2x Laemmli sample buffer were added
707 to the pellets (pellet). Sup and pellet fractions of both seeds and monomeric aSyn A53T were
708 analyzed by SDS-PAGE and Coomassie staining/destaining.

709

710 **Thioflavin T assay**

711 An aliquot of both aSyn A53T seeds and aSyn A53T monomers was thawed at room
712 temperature. For each sample 4 technical replicates were prepared: For each technical
713 replicate either 5 μ l of seeds, monomeric aSyn A53T, or PBS were pipetted into a black 96-
714 well plate (Berthold), respectively. Samples were incubated with 95 μ l of a 25 μ M Thioflavin T
715 (Sigma-Aldrich) in PBS solution for 45 min at room temperature. Fluorometry was performed
716 using a microplate reader (Cytation 5, BioTek, excitation 442 nm, emission 485 nm).

717

718 **Atomic Force Microscopy (AFM)**

719 AFM measurements were conducted on a Bruker Bioscope RESOLV, using Peak Force
720 Tapping Mode at 2 kHz resonant frequency. For liquid AFM measurements a ScanAsyst Fluid+
721 probe from Bruker Nano was run at 0.5 nN setpoint and a peak force amplitude of 90 nm.
722 Freshly cleaved MICA from PLANO was used as a substrate for in situ measurements. Beam
723 alignment was done in the buffer solution. 4 μ l of the target solution was drop cast on the MICA
724 substrate, shortly after (max. 10 s) the volume was filled with 2 ml buffer solution. For dry AFM
725 measurements a ScanAsyst Air probe from Bruker Nano was run at 1.3 nN setpoint and a
726 peak force amplitude of 150 nm. A silicon wafer from PLANO was used as a substrate for dry
727 measurements. 4 μ l of the target solution was spin coated on the Si-substrate at 1000 rpm and
728 air counter flux.

729

730 **Dynamic Light Scattering (DLS)**

731 DLS measurements were performed on a Malvern Instruments Zetasizer Ultra (633 nm laser
732 source), in a 20 μ l quartz cuvette (ZEN2112). The displayed data were recorded over three
733 cycles in back-scattering mode. The total acquisition time was 2 s. Attenuation and position
734 were fixed by the device automatically. The refractive index and absorbance of polystyrene
735 was used.

736

737 **Analysis of Proteotoxic Stress**

738 *Immunocytochemistry*

739 MEFs were cultivated on glass coverslips (Laboratory Glassware Marienfeld). 24 h after
740 seeding, cells were heat stressed at 42°C for 1 h or treated with 0.5 μ M MG-132 for 48 h. Cells
741 were fixed for 15 min with 4 % paraformaldehyde in PBS pH 7.4 and permeabilized with 0.5%
742 (v/v) Triton X-100, 3 mM EDTA pH 8.0 and 5% goat serum in PBS for 30 min at room
743 temperature and then stained with Proteostat® (Enzo Life Sciences, Inc.) at a dilution of 1:2000
744 in 10x assay buffer (ENZO) for 20 min. Cells were then mounted in Fluorshield with DAPI
745 (Sigma). Fluorescence microscopy was performed using a Zeiss ELYRA PS.1 equipped with
746 an LSM880 (Carl Zeiss, Oberkochen) with a 63 x oil immersion objective. Super-resolution

747 images were generated by the Structured Illumination (SIM) technology. SIM confocal images
748 were processed using the ZEN2.1 software (Carl Zeiss, Jena). Data represent the mean \pm SD
749 from $n = 4$ biological replicates. At least 250 cells were assessed per condition. Statistical
750 analysis was carried out using the two-way ANOVA followed by Bonferroni's multiple
751 comparison test to determine significant differences between samples (significance levels: * p
752 ≤ 0.05 ; ** $p \leq 0.01$; *** $p \leq 0.001$).

753 *Trypan blue dye exclusion*

754 Cells were seeded in a 6-well dish at a density of $\sim 500,000$ cells. After 24 h of seeding, cells
755 were either heat stressed at 46°C for 1 h or treated with MG-132 for 16 h ($2 \mu\text{M}$), or 24 h (2
756 μM), or 48 h ($0.5 \mu\text{M}$) and and trypsinized. The cell suspension was centrifuged for 5 min at
757 $100 \times g$ and the cell pellet was then resuspended in PBS. 1 part of cell suspension was mixed
758 with 1 part of trypan blue dye. Trypan blue dye only permeates damaged cell membranes.
759 Therefore, the unstained (viable) and stained (nonviable) cells were counted separately using
760 the hemocytometer. To obtain the total number of viable cells per ml of aliquot, the total number
761 of viable cells were multiplied by 2 (the dilution factor for trypan blue). To obtain the total
762 number of cells per ml of aliquot, the total number of viable and nonviable cells were added up
763 and multiplied by 2. The percentage of viable cells were calculated as follows: Cell viability (%)
764 = (total number of viable cells per ml of aliquot/total number of cells per ml) *100. Data
765 represent the mean \pm SD from $n \geq 5$ biological replicates. Statistical analysis was carried out
766 using the two-way ANOVA followed by Bonferroni's multiple comparison test to determine
767 significant differences between samples (significance levels: * $p \leq 0.05$; ** $p \leq 0.01$; *** $p \leq$
768 0.001).

769 *Immunoblotting*

770 Proteins were size-fractionated by SDS-PAGE (16% or 8% polyacrylamide) and transferred to
771 nitrocellulose by electroblotting. The nitrocellulose membranes were blocked with 5% non-fat
772 dry milk in TBST (tris-buffered saline (TBS) containing 0.1% Tween 20) for 30 min at room
773 temperature and subsequently incubated with the primary antibody against Poly (ADP-ribose)
774 polymerase (PARP) or active caspase-3 in TBST for 16 h at 4°C . After extensive washing with
775 PBST, the membranes were incubated with horseradish peroxidase-conjugated secondary
776 antibody for 1 hour at room temperature. Following washing with PBST, the antigen was
777 detected with the enhanced chemiluminescence detection system.

778 **Phase separation assay**

779 Protein aliquots were thawed on ice. Using Vivaspin 500 columns with 30 or 10 kDa molecular
780 weight cut off (Sartorius Stedim Biotech), the buffer was exchanged to 10 mM Tris, pH 7.4, 1
781 mM DTT by centrifuging five to eight times for 9 min at $12,000 g$, 4°C . After buffer exchange,
782 protein was collected and finally centrifuged at $20,000 g$ for 10 min at 4°C to remove
783 aggregates The final protein concentration was determined by NanoDrop 2000. TEV protease

784 was added to the samples and incubated 1 h for complete cleavage of MBP and 6xHis before
 785 microscopy. After the reaction, 10 μ l of reaction mix was spotted on ibidi coverslip bottom
 786 dishes. The samples were then imaged as maximum intensity projection of a z-stack obtained
 787 using laser scanning microscopy.

788

789 Antibodies

790

Antibody	source	Identifier
Mouse monoclonal anti-HA	BioLegend	Cat# 901502, RRID: AB_2565007
Rabbit polyclonal anti-IKBKG/NEMO	Sigma-Aldrich	Cat# HPA000426, RRID: AB_1851572
Mouse monoclonal anti-IKK γ /NEMO	Cell Signaling Technology	Cat#2695, RIDD: N/A, clone: DA10-12
Rabbit anti-IKK γ /NEMO	Abcam	Ab178872
Rabbit monoclonal anti-linear ubiquitin	Millipore	Cat# MABS199, RRID: AB_2576212
Human monoclonal anti-linear ubiquitin	Genentech	clone: 1F11/3F5/Y102L, ⁴⁴
Mouse monoclonal anti-GFP	Thermo Fisher Scientific	Cat# 14-6674-82, RRID: AB_2572900
Mouse monoclonal anti- α -synuclein	BD Biosciences	Cat# 610787, RRID: AB_398108
Rabbit monoclonal anti- α -synuclein, (phospho Ser129)	Abcam	Cat# ab51253, RRID: AB_869973
Mouse anti- α -synuclein	Santa Cruz Biotechnology	Sc-12767
Mouse anti-phospho-tau	Invitrogen	Cat# MN1020
Mouse anti-TDP-43	Proteintech	Cat# 60019-2-Ig
Rabbit anti-TDP-43	Proteintech	Cat#12892-1-AP
Mouse monoclonal anti β -actin	Sigma-Aldrich	Cat# A5316, RRID: AB_476743
Rabbit polyclonal anti-phospho-IKK α/β (Ser176, Ser180)	Thermo Fisher Scientific	Cat# 710676, RRID: AB_2532752
Rabbit monoclonal anti-NF- κ B p65	Cell Signaling Technology	Cat# 8242, RRID: AB_10859369
Rabbit monoclonal anti-phospho-NF- κ B p65 (Ser536)	Thermo Fisher Scientific	Cat# MA5-15160, RRID: AB_10983078
Rabbit polyclonal anti-p62 / SQSTM1	MBL International	Cat# PM045, RRID: AB_1279301
Mouse monoclonal anti- beta III Tubulin - Neuronal Marker	Abcam	Cat# ab78078, RRID: AB_2256751
Rabbit polyclonal anti-HOIP	Bethyl	Cat# A303-560A, RRID: AB_10949139
Mouse monoclonal anti-Ik β	Cell Signaling Technology	Cat# 4814, RRID: AB_390781
Mouse monoclonal anti-DYKDDDDK Tag (FLAG)	Cell Signaling Technology	Cat# 8146, RRID: AB_10950495
Rabbit monoclonal anti-cleaved caspase-3	Cell Signaling Technology	Cat# 9664
Rabbit polyclonal anti-PARP	Cell Signaling Technology	Cat# 9542
Rabbit monoclonal anti-K63 Ubiquitin	Millipore	Cat# 05-1308, RRID: AB_1587580
Rabbit monoclonal anti-K48 Ubiquitin	Cell Signaling Technology	Cat# 8081, RRID: AB_10859893
Mouse monoclonal anti-pan-Ubiquitin	Santa Cruz Biotechnology	Cat# sc-8017, RRID: AB_628423

791

792 ACKNOWLEDGEMENT

793 We thank Tetsuro Ishii for p62 KO MEFs, Marc Schmidt-Supprian for NEMO KO MEFs, Terje
 794 Johansen for p62 plasmids, Sascha Martens for mCherry-p62, Yen-Ting Chen for discussing
 795 protein adsorption processes, and Genentech for the 1F11/3F5/Y102L antibody. This work
 796 was supported by the German Research Foundation (WI/2111-4, WI/2111-6, WI/2111-8, FOR
 797 2848 to KFW) and Germany's Excellence Strategy - EXC 2033 - 390677874 – RESOLV (to
 798 KFW and JT). SR-SIM microscopy was funded by the German Research Foundation and the
 799 State Government of North Rhine-Westphalia (INST 213/840-1 FUGG).

800

801 AUTHOR CONTRIBUTIONS

802 **Nikolas Furthmann:** Conceptualization; Data curation; Formal analysis; Validation;
 803 Investigation; Visualization; Methodology; Writing—original draft;

804 **Lena Angersbach:** Conceptualization; Data curation; Formal analysis; Validation;
805 Investigation; Visualization; Methodology;
806 **Verian Bader:** Conceptualization; Data curation; Formal analysis; Validation; Investigation;
807 Visualization; Methodology; Writing—original draft;
808 **Alina Blusch:** Formal analysis; Validation; Investigation; Visualization; Methodology;
809 Writing—original draft;
810 **Simran Goel:** Formal analysis; Validation; Investigation; Visualization; Methodology; Writing—
811 original draft;
812 **Ana Sánchez-Vicente:** Conceptualization; Formal analysis; Validation; Investigation;
813 Visualization; Methodology; Writing—original draft;
814 **Laura J. Krause:** Resources; Writing – review & editing
815 **Perna Grover:** Formal analysis; Validation; Investigation;
816 **Victoria A. Trinkaus:** Validation; Investigation; Visualization; Methodology;
817 **Eva M. van Well:** Formal analysis; Validation; Investigation;
818 **Maximilian Jaugstetter:** Formal analysis; Validation; Investigation; Visualization;
819 Methodology;
820 **Kristina Tschulik:** Resources; Writing – review & editing
821 **Rune B. Daamgard:** Resources; Writing – review & editing
822 **Carsten Saft:** Resources;
823 **Gisa Ellrichmann:** Resources;
824 **Arend Koch:** Resources;
825 **Benjamin Englert:** Resources;
826 **Marcus Glatzel:** Resources; Writing – review & editing
827 **F. Ulrich Hartl:** Resources; Writing – review & editing
828 **Ken Nakamura:** Resources; Writing – review & editing
829 **Chadwick W. Christine:** Resources; Writing – review & editing
830 **Eric J. Huang:** Investigation; Visualization; Methodology; Resources; Writing – review &
831 editing
832 **Jörg Tatzelt:** Conceptualization; Supervision; Validation; Visualization; Writing—original draft;
833 Project administration;
834 **Konstanze F. Winklhofer:** Conceptualization; Supervision; Funding acquisition; Validation;
835 Visualization; Writing—original draft; Project administration;
836
837 **CONFLICT OF INTEREST**
838 RBD is a scientific advisor for Immagine B.V.
839
840 **FIGURE LEGENDS**

841 **Figure 1. NEMO is associated with pathological protein aggregates.**

842 **A. Widespread mixed brain proteinopathy in a patient expressing mutant Q330X NEMO.**

843 Both low and high magnification images show the presence of aggregated proteins, such as
844 α -synuclein, hyperphosphorylated tau, TDP-43, and amyloid beta in different brain regions.
845 Many structures resembling Lewy body and Lewy neurites in pigmented neurons in the
846 substantia nigra pars compacta (SNpc) are positive in immunostaining for α -synuclein,
847 hyperphosphorylated tau, and ubiquitin.

848 **B. Domain structure of wildtype (WT) human NEMO and mutant Q330X NEMO.** DD,
849 dimerization domain; CC1, coiled coil 1 domain; CC2, coiled coil 2 domain; UBAN, ubiquitin
850 binding in ABIN and NEMO; LZ, leucine zipper; ZF, zinc finger.

851 **C, D. M1-linked ubiquitin and NEMO colocalize with α -synuclein, tau, and TDP-43**
852 **aggregates in human brain.** Immunofluorescent stainings of cortical or midbrain sections

853 from patients with Parkinson's disease (PD), Alzheimer's disease (AD), or frontotemporal
854 dementia (FTD). Brain sections were stained with antibodies against M1-ubiquitin (C), NEMO
855 (D), and α -synuclein (PD), tau (AD), or TDP-43 (FTD). Scale bar, 10 μ m.

856

857 **Figure 2. NEMO protects from proteotoxic stress.**

858 **A, B. NEMO-deficient cells are prone to protein aggregation under proteotoxic stress.**

859 **A.** NEMO wildtype (WT) and knockout (KO) mouse embryonic fibroblasts (MEFs) were heat
860 stressed (42°C, 1 h) or treated with the proteasomal inhibitor MG-132 (0.5 μ M, 48 h) and then
861 stained by Proteostat[®] to detect protein aggregates. Scale bar: 20 μ m **B.** Cells positive for
862 aggregates were quantified. All data are displayed as mean \pm SD based on 4 independent
863 experiments, analyzed by two-way ANOVA followed by Bonferroni's multiple comparison test.
864 At least 250 cells were assessed per condition.

865 **C, D. Wildtype NEMO but not Q330X NEMO decreases misfolding of the folding sensor**

866 **FlucDM-EGFP-luciferase.** NEMO KO MEFs transiently expressing FlucDM-EGFP-luciferase
867 and either wildtype (WT) NEMO or Q330X NEMO were subjected to a heat stress (HS, 43°C,
868 20 min) 48 h after transfection or left untreated. **C.** The cells were then analyzed by
869 immunocytochemistry and fluorescence microscopy. Shown is the fraction of NEMO-
870 expressing cells with EGFP-positive foci. Data represent mean \pm SEM based on 3 independent
871 experiments. At least 900 transfected cells have been analyzed per condition. Statistics: one-
872 tailed Mann Whitney U-tests * $p \geq 0.05$. **D.** In parallel, luciferase activity of control and heat
873 stressed cells were analyzed luminometrically. Data represent mean \pm SEM based on 7
874 independent experiments. Statistics: One-way ANOVA with Bonferroni's Multiple Comparison
875 posthoc test; *** $p \leq 0,001$.

876 **E, F. Transient heat stress does not activate NF- κ B signaling.** **E.** HEK293T transiently

877 expressing an NF- κ B luciferase reporter construct were heat stressed for 20, 40, or 60 min

878 (42°C) and 8 h later luciferase activity was quantified. As a positive control, one set of cells
879 was treated with TNF (10 ng/ml, 8 h). Data are shown as normalized mean \pm SD based on 4
880 independent experiments. **F.** SH-SY5Y cells were heat stressed (42°C) for the indicated time
881 and then nuclear translocation of the NF- κ B subunit p65 was analyzed by
882 immunocytochemistry and fluorescence microscopy using antibodies against p65. As a
883 positive control, one set of cells was treated with TNF (25 ng/ml, 15 min).

884

885 **Figure 3. NEMO and LUBAC components are recruited to aSyn aggregates.**

886 **A. M1-linked ubiquitin is enriched at aSyn aggregates formed in the cellular aSyn**
887 **seeding model.** SH-SY5Y cells stably expressing aSyn A53T-GFP were treated with aSyn
888 A53T seeds, fixed 72 h after seeding, and analyzed by immunocytochemistry and fluorescence
889 SR-SIM using M1-ubiquitin-specific antibodies. Scale bar, 20 and 5 μ m.

890 **B. M1-linked ubiquitin colocalizes with pS129-aSyn-positive neurites in primary**
891 **neurons.** Primary cortical mouse neurons were treated with aSyn A53T seeds at day 5 *in vitro*
892 to induce aggregation of endogenous aSyn, fixed 7 days (rows 1 and 2) or 10 days (rows 3
893 and 4) after seeding, and analyzed by immunocytochemistry and fluorescence SR-SIM using
894 antibodies against pS129-aSyn, M1-linked ubiquitin, and β III-Tubulin. Scale bar, 20 and 5 μ m.

895 **C. M1-linked ubiquitin co-immunoprecipitates with aSyn.** SH-SY5Y cells stably expressing
896 A53T-GFP aSyn were treated with aSyn A53T seeds for 72 h, lysed in 1% Triton X-100 in
897 PBS, and aSyn-GFP was immunoprecipitated using GFP-trap beads. An immunoprecipitation
898 with anti-HA beads was used to control for nonspecific binding. The pellet was analyzed by
899 immunoblotting for M1-linked ubiquitin and GFP. The input was immunoblotted against aSyn
900 and β -actin.

901 **D. Endogenous NEMO is enriched at aSyn aggregates.** SH-SY5Y cells stably expressing
902 aSyn A53T-GFP were treated as described in A and analyzed by immunocytochemistry and
903 fluorescence SR-SIM using antibodies against NEMO and M1-linked ubiquitin. Scale bar, 20
904 and 5 μ m.

905 **E. LUBAC components are recruited to aSyn aggregates.** SH-SY5Y cells stably expressing
906 α -Synuclein A53T-GFP were transiently transfected with plasmids encoding either HA-HOIP,
907 HA-HOIL 1L, or HA-SHARPIN, or HA-HHARI as a control. One day after transfection, the cells
908 were treated with aSyn A53T seeds, fixed 48 h after seeding, and analyzed by
909 immunocytochemistry and fluorescence SR-SIM using antibodies against the HA-tag. Scale
910 bar, 20 and 5 μ m.

911

912 **Figure 4. In contrast to Q330X NEMO, WT NEMO is recruited to pathological protein**
913 **aggregates and increases the abundance of M1-linked ubiquitin**

914 **A. In contrast to WT NEMO, Q330X NEMO is not present at aSyn aggregates.** SH-SY5Y
915 cells stably expressing aSyn A53T-GFP were transiently transfected with either HA-tagged WT
916 NEMO (left panel) or HA-tagged Q330X HA-NEMO (right panel). After 24 h, the cells were
917 treated with aSyn A53T seeds, fixed 48 h after seeding, and analyzed by immunocytochemistry
918 and fluorescence SR-SIM using an antibody against the HA-tag. Scale bar, 20 and 5 μ m.

919 **B. Q330X NEMO is not recruited to Htt-Q97-GFP aggregates.** SH-SY5Y cells were
920 transiently transfected with Htt-Q97-GFP and either HA-tagged WT NEMO (left panel) or HA-
921 tagged Q330X NEMO (right panel). Cells were fixed after 72 h and analyzed by
922 immunocytochemistry and fluorescence SR-SIM using antibodies against the HA-tag. Scale
923 bar, 20 and 5 μ m.

924 **C. Q330X NEMO does not bind to M1-linked ubiquitin.** HEK293T cells were transiently
925 transfected with either WT HA-NEMO or Q330X HA-NEMO. After 24 h, the cells were lysed
926 and lysates were incubated with recombinant M1-linked tetra-ubiquitin (4xM1-ub) for 2 h at
927 4°C. NEMO was immunoprecipitated using anti-HA beads. Immunoprecipitated NEMO was
928 immunoblotted using antibodies against M1-linked ubiquitin. The input was immunoblotted for
929 M1-linked ubiquitin, NEMO and β -actin.

930 **D. Q330X NEMO is not M1-ubiquitinated upon TNF treatment or increased LUBAC**
931 **expression.** HEK293T cells were transiently transfected with WT HA-NEMO or Q330X HA-
932 NEMO +/- LUBAC (HOIP + HOIL-1L + SHARPIN) as indicated. After 24 h, one set of cells was
933 treated with TNF (25 ng/ml, 30 min) to stimulate linear ubiquitination. After cell lysis under
934 denaturing conditions, NEMO was immunoprecipitated using anti-HA beads.
935 Immunoprecipitated NEMO was immunoblotted using antibodies against M1-linked ubiquitin.
936 The input was immunoblotted for NEMO and β -actin.

937 **E. In contrast to WT NEMO, Q330X NEMO does not co-immunoprecipitate with**
938 **endogenous HOIP.** HEK293T cells were transiently transfected with either WT HA-NEMO or
939 Q330X HA-NEMO. After cell lysis, NEMO was immunoprecipitated using anti-HA beads. Anti-
940 c-myc beads were used to control for nonspecific binding. Immunoprecipitated NEMO was
941 immunoblotted for endogenous HOIP. The input was immunoblotted for HOIP, NEMO, and β -
942 actin.

943 **F, G. M1-ubiquitin chains at aSyn aggregates are increased by WT but not Q330X NEMO.**
944 CRISPR/Cas9 NEMO KO SH-SY5Y cells were transiently transfected with aSyn A53T-GFP
945 and either WT NEMO or Q330X NEMO. One day after transfection, the cells were treated with
946 aSyn A53T seeds, and fixed 48 h after seeding and analyzed by immunohistochemistry and
947 fluorescence SR-SIM using anti-antibodies against aSyn, M1-ubiquitin and NEMO.
948 Colocalization of M1-ubiquitin and aSyn aggregates (F) or M1-ubiquitin, NEMO and aSyn
949 aggregates (G) was quantified using the Pearson colocalization coefficient. **F.** Data are
950 displayed as mean \pm SEM. n = 16, 16. Statistics: two-tailed Mann-Whitney U-test ***p \geq 0.001.

951 **G.** Data are displayed as mean \pm SEM. n = 18, 23. Statistics: two-tailed student's t-test. ***p \geq
952 0.001.

953

954 **Figure 5. A local NF- κ B signaling platform is assembled at aSyn aggregates that does**
955 **not promote nuclear translocation of p65.**

956 **A. IKK α / β and p65 are recruited to aSyn aggregates.** SH-SY5Y cells stably expressing aSyn
957 A53T-GFP were treated with aSyn A53T seeds, fixed on day 3 after seeding, and analyzed by
958 immunocytochemistry and fluorescence SR-SIM using antibodies against phospho-IKK α / β ,
959 p65, phospho-p65, and M1-linked ubiquitin. Scale bar, 20 and 5 μ m.

960 **B, C. Assembling of an NF- κ B signaling platform at aSyn aggregates does not result in**
961 **p65 nuclear translocation and impairs TNF-induced NF- κ B activation.** **B.** Samples were
962 prepared as described in A, treated with TNF for 15 min (25 ng/ml) on day 1, 2, or 3 days after
963 seeding, fixed and quantified for nuclear translocation of p65 by immunocytochemistry and
964 fluorescence confocal microscopy using antibodies against p65. For the seeded samples, only
965 cells with aSyn aggregates were used for quantification. Data represent the means \pm SD of
966 five independent experiments. Statistics: One-way ANOVA followed by Tukey's multiple
967 comparison test. **C.** Representative immunofluorescence images of the experiment described
968 in B (day 2 after seeding). Scale bar, 20 μ m.

969 **D. TNF-induced p65 nuclear translocation is impaired in cells with Htt-polyQ**
970 **aggregates.** SH-SY5Y cells were transiently transfected with GFP-tagged Htt-25Q or Htt-Q97
971 and either vector (co), wildtype HOIP or catalytically inactive C885A HOIP, as indicated. On
972 day 3 after transfection, the cells were treated with TNF (20 ng/ml, 20 min) and nuclear
973 translocation of p65 was analyzed by as described in B. Expression of HOIP was analyzed by
974 immunoblotting, actin was used as input control. Data represent the means \pm SD of three
975 independent experiments each performed in triplicates. At least 600 transfected cells were
976 assessed per condition. Statistics: One-way ANOVA with Tukey's Multiple Comparison
977 posthoc test; ***p \leq 0,001.

978

979 **Figure 6. NEMO decreases the number of cells with aSyn aggregates in a p62-dependent**
980 **manner.**

981 **A. WT NEMO but neither Q330X NEMO nor D311N NEMO decreases the number of cells**
982 **with aSyn aggregates.** SH-SY5Y cells stably expressing aSyn A53T-GFP were transiently
983 transfected with either HA-NEMO, Q330X HA-NEMO, D311N HA-NEMO, or mCherry as a
984 control and treated with aSyn A53T seeds 24 h after transfection. The cells were treated 16 h
985 after seeding with Bafilomycin A1 (Baf, 25 nM). 40 h after seeding, the cells were fixed and
986 analyzed by immunocytochemistry and fluorescence microscopy using anti-HA antibodies.
987 The fraction of HA- or mCherry-positive cells containing aSyn-GFP aggregates was quantified.

988 Data are shown as mean \pm SD based on 5 independent experiments. At least 750 cells per
989 condition were quantified. Statistics were applied to the entire dataset. For better comparability,
990 the control is shown for each NEMO construct. Statistics: One-way ANOVA followed by
991 Tukey's multiple comparison test. *** $p \leq 0,001$.

992 **B. Catalytically active HOIP decreases the number of cells with aSyn aggregates.** SH-
993 SY5Y cells stably expressing aSyn A53T-GFP were transiently transfected with either WT HA-
994 HOIP, catalytically inactive C885A HA-HOIP, or mCherry as a control, and treated as
995 described in A. The fraction of HA- or mCherry-positive cells containing aSyn-GFP aggregates
996 was quantified. Data are shown as mean \pm SD based on 5 independent experiments. At least
997 750 cells per condition were quantified. Statistics were applied to the entire dataset. For better
998 comparability, the control is shown for each NEMO construct. Statistics: One-way ANOVA
999 followed by Tukey's multiple comparison test. *** $p \leq 0,001$.

1000 **C. p62 is present at aSyn aggregates.** SH-SY5Y cells stably expressing aSyn A53T-GFP
1001 were treated with aSyn A53T seeds, fixed 72 h after seeding, and analyzed by
1002 immunocytochemistry and SR-SIM fluorescence microscopy using anti-p62 antibodies. Scale
1003 bar, 20 and 5 μm .

1004 **D. p62 co-immunoprecipitates with WT NEMO but not with Q330X NEMO.** HEK293T cells
1005 were transiently transfected with either WT HA-NEMO, Q330X HA-NEMO, or WT FLAG-
1006 NEMO to control for unspecific binding. After cell lysis, HA-tagged proteins were
1007 immunoprecipitated using anti-HA-beads. Immunoprecipitated proteins were immunoblotted
1008 using antibodies against p62, M1-linked ubiquitin, and NEMO. The input was immunoblotted
1009 for p62, NEMO, and β -actin.

1010 **E. NEMO and HOIP reduce the number of aSyn aggregates in a p62-dependent manner,**
1011 **which requires the UBA domain of p62.** p62 KO MEFs were transiently transfected with
1012 aSyn A53T-GFP, HA-NEMO, HA-HOIP or mCherry as a control, and p62 or p62 Δ UBA, as
1013 indicated. One day after transfection, the cells were treated aSyn A53T seeds, and fixed 48 h
1014 after seeding. The fraction of cells containing aSyn aggregates was quantified as described in
1015 A. Statistics: One-way ANOVA followed by Tukey's multiple comparison test. ** $p \leq 0,01$, *** p
1016 $\leq 0,001$.

1017 **F. The p62-dependent effect of NEMO on aSyn aggregates is sensitive to lysosomal**
1018 **inhibition.** p62 KO MEFs were transiently transfected with aSyn A53T-GFP and HA-NEMO,
1019 or HA-NEMO and p62, or mCherry as a control, as indicated. The next day, cells were treated
1020 with aSyn A53T seeds, and after 16 h treated with Bafilomycin A1 (Baf, 25 nM). 40 h after
1021 seeding, cells were fixed and the fraction of cells containing aSyn aggregates was quantified
1022 as described in A. Statistics: One-way ANOVA followed by Tukey's multiple comparison test.
1023 ** $p \leq 0,01$, *** $p \leq 0,001$.

1024

1025 **Figure 7. p62 binds to aSyn aggregates in a NEMO-dependent manner.**
1026 **A, B, C. Colocalization of p62 and aSyn aggregates is decreased in the Q330X NEMO**
1027 **patient brain despite increased p62 expression. A.** Paraffin-embedded brain sections from
1028 control, DLBL (Dementia with Lewy Bodies) or the Q330X NEMO patient brain were analyzed
1029 by immunohistochemistry and fluorescence SR-SIM using antibodies against aSyn and p62.
1030 Scale bar, 200 μm **B.** Foci staining positive for both aSyn and p62 were quantified in 28-30
1031 fields of view per brain section. **C.** Foci staining positive for p62 only were quantified in 10
1032 fields of view per brain section. Data are displayed as mean \pm SEM. Statistics: Kruskal-Wallis
1033 test followed by Tuckey's multiple comparison test. *** $p \geq 0.001$.
1034 **D, E. Colocalization of p62 and aSyn aggregates is decreased in NEMO KO SH-SY5Y**
1035 **cells. D.** CRISPR/Cas9 NEMO KO or WT SH-SY5Y cells were transiently transfected with
1036 aSyn A53T-GFP. One day after transfection, the cells were treated aSyn A53T seeds, and
1037 fixed 48 h after seeding and analyzed by immunohistochemistry and fluorescence SR-SIM
1038 using anti-antibodies against aSyn and p62. Scale bar = 10 μm **E.** Colocalization of aSyn-GFP
1039 and endogenous p62 was quantified using the Pearson colocalization coefficient. Data are
1040 displayed as mean \pm SEM. n = 18-23 Statistics: two-tailed student's t-test. ** $p \geq 0.01$.
1041

1042 **Figure 8. NEMO promotes p62 local concentration by co-condensation with M1-linked**
1043 **ubiquitin.**

1044 **A, B.** Foci-like concentration of p62 at aSyn aggregates is reduced in NEMO-deficient cells.
1045 **A.** CRISPR/Cas9 NEMO KO or WT HeLa cells were transiently transfected with aSyn A53T-
1046 GFP. One day after transfection, the cells were treated with aSyn A53T seeds, fixed 48 h after
1047 seeding and analyzed by immunohistochemistry and fluorescence 3D SR-SIM using anti-
1048 antibodies against p62. Scale bar, 1 μm . Coverage of aSyn-GFP aggregates by p62 was
1049 analyzed using the Imaris 10.0 surface modules and a surface-to-surface MatLab Plugin. **B.**
1050 The p62 coverage of the reconstructed aSyn-GFP surface was quantified and plotted as
1051 percentage of the total aSyn-GFP aggregate surface. Data are displayed as mean \pm SEM. n =
1052 10-12 Statistics: two-tailed student's t-test. ** $p \geq 0.01$.
1053 **C. NEMO forms a mobile phase at aSyn aggregates.** CRISPR/Cas9 NEMO KO HeLa cells
1054 were transiently transfected with aSyn A53T-GFP and NEMO-Halo7. One day after
1055 transfection the cells were incubated with aSyn A53T seeds for 48 h. For labelling of the Halo
1056 tag, the cells were incubated for 30 min with 2.5 μM TMR dye and washed for 30 min with cell
1057 culture medium prior to live cell imaging. Fluorescence recovery after photobleaching (FRAP)
1058 was performed by 5 consecutive bleaching pulses using the 561 nm laser at 100% intensity
1059 within a defined region of interest (white circle) at a aSyn-GFP protein aggregate (green
1060 outline). Fluorescence recovery was measured for 5 min and plotted as a percentage of
1061 baseline fluorescence. n = 9. Scale bar, 1 μm .

1062 **D. p62 colocalizes with NEMO and M1-linked ubiquitin at aSyn aggregates.** HeLa cells
1063 were transiently transfected with aSyn A53T-GFP. One day after transfection, the cells were
1064 treated with aSyn A53T seeds, and fixed 48 h after seeding and analyzed by
1065 immunohistochemistry and fluorescence SR-SIM using anti-antibodies against p62, NEMO
1066 and M1-ubiquitin (all at endogenous expression). Shown are representative images of p62 co-
1067 localizing with NEMO (left panel) and p62 colocalizing with M1-ubiquitin (right panel) at aSyn-
1068 GFP aggregates. Scale bar, 1 μm .

1069 **E. p62 and NEMO co-condensate in the presence of M1-linked polyubiquitin.** 2.5 μM
1070 recombinant mCherry-p62 (red) mixed with 5 μM recombinant wildtype NEMO-GFP (green)
1071 were supplemented with M1-linked ubiquitin to induce phase separation. Top lane: No M1-
1072 linked ubiquitin added. Middle lane: 2.5 μM M1-linked tetra-ubiquitin (4 \times M1-ub). Bottom lane:
1073 1.0 μM M1-linked octa-ubiquitin (8 \times M1-ub). Shown are laser scanning microscopy images.
1074 Scale bar, 10 μm .

1075 **F. NEMO reduces the threshold concentrations required for ubiquitin-dependent p62**
1076 **phase separation.** Phase diagrams depicting concentration-dependent phase separation of
1077 p62 and M1-linked octa- or tetra-ubiquitin (8 \times M1-ub or 4 \times M1-ub) with or without 5 μM
1078 recombinant wildtype NEMO. p62 was incubated in presence of recombinant M1-linked
1079 ubiquitin at the concentrations indicated and analyzed by laser scanning microscopy. Black
1080 empty circles: no phase separation; red/yellow solid circles: phase separation.

1081

1082 **Figure S1. The Q330X NEMO mutant is defective in NF- κ B signaling.**

1083 **A, B. The Q330X mutation disrupts binding of NEMO to I κ B α but not to IKK β .** HEK293T
1084 cells were transiently transfected with wildtype FLAG-NEMO or Q330X FLAG-NEMO and HA-
1085 I κ B α (A) or HA-IKK β (B) as indicated. One day after transfection, the cells were lysed and HA-
1086 tagged proteins were immunoprecipitated using anti-HA-beads followed by immunoblotting
1087 using antibodies against NEMO. The input was immunoblotted for NEMO, I κ B α (A) or IKK β
1088 (B) and β -actin.

1089 **C. WT NEMO but not Q330X NEMO rescues defective I κ B α degradation in NEMO KO**
1090 **MEFs.** WT and NEMO KO MEFs were transiently transfected with WT FLAG-NEMO, Q330X
1091 FLAG-NEMO or luciferase as a control. One day after transfection, the cells were treated with
1092 TNF (25 ng/ml, 15min) as indicated or left untreated and analyzed by immunoblotting using
1093 antibodies against I κ B α , NEMO and β -actin.

1094 **D. In contrast to WT NEMO, Q330X NEMO does not promote NF- κ B transcriptional**
1095 **activity.** WT and NEMO KO MEFs were transiently transfected with an NF- κ B luciferase
1096 reporter plasmid and WT FLAG-NEMO, Q330X FLAG-NEMO, or EGFP as a control. 24 h after
1097 transfection, the cells were lysed and luciferase activity was measured luminometrically using
1098 a plate reader. Data represent the means \pm SEM of three independent experiments consisting

1099 of three technical replicates each. Statistics: Student's t-test. Lower panel: Cell lysates were
1100 immunoblotted using antibodies against NEMO and β -actin (input control).

1101

1102 **Figure S2. NEMO KO MEFs are more vulnerable to proteotoxic stress.**

1103 **A. NEMO deficiency decreases cell viability upon proteasomal inhibition.** WT and NEMO
1104 KO MEFs were treated with MG-132 for 16 h (2 μ M), 24 h (2 μ M), or 48 h (0.5 μ M), or kept
1105 untreated. Cell viability was quantified using Trypan blue dye exclusion. Data are displayed as
1106 mean \pm SD and were analyzed by two-way ANOVA followed by Bonferroni's multiple
1107 comparison test, n=6.

1108 **B. NEMO deficiency increases apoptotic cell death upon proteasomal inhibition.** WT and
1109 NEMO KO MEFs were treated with MG-132 (2 μ M, 24 h) and then analyzed by immunoblotting
1110 using antibodies against PARP and active caspase-3. The input was immunoblotted for β -
1111 actin.

1112 **C. NEMO deficiency decreases cell viability upon heat stress.** WT and NEMO KO MEFs
1113 were subjected to a heat stress (46°C, 1 h), followed by overnight recovery. Cell viability was
1114 quantified using Trypan blue dye exclusion. Data are displayed as mean \pm SD and were
1115 analyzed by two-way ANOVA followed by Bonferroni's multiple comparison test, n=5.

1116

1117 **Figure S3. aSyn A53T seeds induce aggregation of pS129-positive aSyn-GFP**
1118 **aggregates that colocalize with M1-linked ubiquitin.**

1119 **A. aSyn-GFP aggregates are phosphorylated at S129 and are modified by M1-linked**
1120 **ubiquitin.** SH-SY5Y cells stably expressing aSyn A53T-GFP were treated with aSyn A53T
1121 seeds (+ seeds) or PBS as a control, fixed 24 h, 48 h, or 72 h after seeding, and analyzed by
1122 immunocytochemistry and fluorescence SR-SIM using antibodies against pS129-aSyn and
1123 M1-linked ubiquitin. Scale bar, 20 μ m.

1124 **B. aSyn A53T seeds induce aggregation and phosphorylation of aSyn-GFP at S129.** SH-
1125 SY5Y cells stably expressing aSyn A53T-GFP were treated with aSyn A53T seeds or PBS as
1126 a control and harvested 24 h, 48 h, or 72 h after seeding. The cells were subjected to a
1127 detergent solubility assay and analyzed by immunoblotting using antibodies against pS129-
1128 aSyn, aSyn, and β -actin.

1129 **C. aSyn A53T seeds induce the formation of immobile aSyn-GFP aggregates.** SH-SY5Y
1130 cells stably expressing aSyn A53T-GFP were treated with aSyn A53T seeds and GFP
1131 aggregates in living cells were analyzed by FRAP (fluorescence recovery after photobleaching)
1132 72 h after seeding. An area in the middle and at the edge of an aSyn aggregate was
1133 photobleached. Representative images are shown in the upper panel. Scale bar, 5 μ m.
1134 Normalized intensities of the FRAP experiments are shown in the lower panel. All data are
1135 displayed as mean, n=3.

1136

1137 **Figure S4. Validation of aSyn A53T seeds.**

1138 **A. Sedimentation assay for monomeric aSyn A53T and aSyn A53T seeds.** *In vitro* formed
1139 aSyn A53T seeds were separated from soluble aSyn A53T monomers by centrifugation.
1140 Supernatant (sup) and pellet fractions were analyzed by SDS-PAGE and Coomassie staining.

1141 **B. aSyn A53T seeds bind to Thioflavin T.** Fluorometry of monomeric aSyn, aSyn seed or
1142 PBS as a control was performed using a microplate reader. Data are shown as mean \pm SD,
1143 $n=4$ technical replicates for each sample.

1144 **C. Derived hydrodynamic diameter of aSyn A53T seeds measured by dynamic light
1145 scattering (DLS).** The size distribution of freshly sonicated aSyn A53T seeds dispersed in
1146 PBS was evaluated from the derived intensity, considering the number distribution of colloids.
1147 A mean diameter of 27.7 nm with a standard deviation of 5.7 nm was derived from a Gaussian
1148 fit.

1149 **D. Analysis of aSyn A53T seeds by atomic force microscopy (AFM).** 3D rendered image
1150 of a single aSyn A53T seed adsorbed on MICA from a freshly sonicated dispersion of aSyn
1151 A53T seeds in PBS, measured by liquid AFM in peak force mode. Rendering was done on a
1152 240x240 nm height sensor image by NanoScope Analysis software from Bruker. The
1153 measured feature exhibits a vertical length of 59 nm, a horizontal length of 41 nm and a
1154 maximum height of 10 nm.

1155 **E. aSyn size distribution of LAFM height measurements on MICA in PBS solution.**
1156 Obtained 2D mapping of the measured surface (Top: size 6.6 x 6.6 μm). Particle size
1157 distribution was derived by particle analysis mode of the Bruker Nanoscope software: Height
1158 threshold was set to > 5 nm. Statistical distribution was evaluated with a Log normal function:
1159 Mean particle diameter 32.1 ± 10.2 nm.

1160 **F. aSyn size distribution of AFM height measurements on Si-wafer after 4 μl
1161 dropcasting.** Obtained 2D mapping of the measured surface (Top: size 6.6 x 6.6 μm). Particle
1162 size distribution was derived by particle analysis mode of the Bruker Nanoscope software:
1163 Height threshold was set to > 16 nm. Statistical distribution was evaluated with a Lognormal
1164 function: Mean particle diameter 28.7 ± 10.0 nm.

1165

1166 **Figure S5. Impaired recruitment of D311N NEMO and p62 Δ UBA to aSyn aggregates.**

1167 **A. D311N NEMO is not recruited to aSyn aggregates.** SH-SY5Y cells stably expressing
1168 aSyn A53T-GFP were transiently transfected with D311N HA-NEMO. After 24 h, the cells were
1169 treated with aSyn A53T seeds, fixed 48 h after seeding, and analyzed by immunocytochemistry
1170 and fluorescence SR-SIM using an antibody against the HA-tag. Scale bar, 20 and 5 μm .

1171 **B. Modification of NEMO Q330X with ubiquitin is impaired.** HEK293T cells were transiently
1172 transfected with plasmids encoding HA-tagged wildtype NEMO, Q330X NEMO, or D311N

1173 NEMO. Cells were lysed under denaturing conditions and the HA-tag was immunoprecipitated
1174 using anti-HA agarose; anti-myc-agarose served as a control for unspecific binding. Samples
1175 were analyzed by immunoblotting with antibodies specific for M1-, K63-, K48-linked, or pan-
1176 ubiquitin.

1177 **C. Recruitment of p62 lacking the UBA domain aSyn aggregates is impaired.** SH-SY5Y
1178 cells stably expressing aSyn A53T-GFP were transiently transfected with plasmids encoding
1179 either HA-tagged p62 or p62 Δ UBA as indicated. After 24 h, the cells were treated with aSyn
1180 A53T seeds, fixed 48 h later, and analyzed by immunocytochemistry and fluorescence SR-
1181 SIM using an antibody against the HA-tag. Scale bar, 20 and 5 μ m.

1182

1183 REFERENCES

1184 1. Kwon YT, Ciechanover A. The Ubiquitin Code in the Ubiquitin-Proteasome System and
1185 Autophagy. *Trends Biochem Sci* **42**, 873-886 (2017).

1186

1187 2. Johnston HE, Samant RS. Alternative systems for misfolded protein clearance: life
1188 beyond the proteasome. *Febs J* **288**, 4464-4487 (2021).

1189

1190 3. Le Guerroue F, Youle RJ. Ubiquitin signaling in neurodegenerative diseases: an
1191 autophagy and proteasome perspective. *Cell Death Differ* **28**, 439-454 (2021).

1192

1193 4. Lei L, Wu Z, Winklhofer KF. Protein quality control by the proteasome and autophagy:
1194 A regulatory role of ubiquitin and liquid-liquid phase separation. *Matrix Biol*, (2020).

1195

1196 5. Pohl C, Dikic I. Cellular quality control by the ubiquitin-proteasome system and
1197 autophagy. *Science* **366**, 818-822 (2019).

1198

1199 6. Yin Z, Popelka H, Lei Y, Yang Y, Klionsky DJ. The Roles of Ubiquitin in Mediating
1200 Autophagy. *Cells* **9**, (2020).

1201

1202 7. Swatek KN, Komander D. Ubiquitin modifications. *Cell Res* **26**, 399-422 (2016).

1203

1204 8. Yau R, Rape M. The increasing complexity of the ubiquitin code. *Nat Cell Biol* **18**, 579-
1205 586 (2016).

1206

1207 9. Oh E, Akopian D, Rape M. Principles of Ubiquitin-Dependent Signaling. *Annu Rev Cell*
1208 *Dev Biol* **34**, 137-162 (2018).

1209

- 1210 10. Dikic I, Schulman BA. An expanded lexicon for the ubiquitin code. *Nat Rev Mol Cell*
1211 *Biol*, 1-15 (2022).
1212
- 1213 11. Kirisako T, *et al.* A ubiquitin ligase complex assembles linear polyubiquitin chains.
1214 *Embo J* **25**, 4877-4887 (2006).
1215
- 1216 12. Iwai K. Discovery of linear ubiquitination, a crucial regulator for immune signaling and
1217 cell death. *Febs J* **288**, 1060-1069 (2021).
1218
- 1219 13. Fiil BK, Gyrd-Hansen M. The Met1-linked ubiquitin machinery in inflammation and
1220 infection. *Cell Death Differ* **28**, 557-569 (2021).
1221
- 1222 14. Fuseya Y, Iwai K. Biochemistry, Pathophysiology, and Regulation of Linear
1223 Ubiquitination: Intricate Regulation by Coordinated Functions of the Associated Ligase
1224 and Deubiquitinase. *Cells* **10**, (2021).
1225
- 1226 15. Jahan AS, Elbaek CR, Damgaard RB. Met1-linked ubiquitin signalling in health and
1227 disease: inflammation, immunity, cancer, and beyond. *Cell Death Differ* **28**, 473-492
1228 (2021).
1229
- 1230 16. Oikawa D, Sato Y, Ito H, Tokunaga F. Linear Ubiquitin Code: Its Writer, Erasers,
1231 Decoders, Inhibitors, and Implications in Disorders. *Int J Mol Sci* **21**, (2020).
1232
- 1233 17. Dittmar G, Winklhofer KF. Linear Ubiquitin Chains: Cellular Functions and Strategies
1234 for Detection and Quantification. *Front Chem* **7**, 915 (2019).
1235
- 1236 18. Rittinger K, Ikeda F. Linear ubiquitin chains: enzymes, mechanisms and biology. *Open*
1237 *Biol* **7**, (2017).
1238
- 1239 19. Hrdinka M, Gyrd-Hansen M. The Met1-Linked Ubiquitin Machinery: Emerging Themes
1240 of (De)regulation. *Mol Cell* **68**, 265-280 (2017).
1241
- 1242 20. Tokunaga F, Ikeda F. Linear ubiquitination in immune and neurodegenerative
1243 diseases, and beyond. *Biochem Soc Trans*, (2022).
1244
- 1245 21. Shibata Y, Komander D. Lubac. *Curr Biol* **32**, R506-R508 (2022).
1246

- 1247 22. Spit M, Rieser E, Walczak H. Linear ubiquitination at a glance. *J Cell Sci* **132**, (2019).
1248
- 1249 23. Zinngrebe J, Walczak H. TLRs Go Linear - On the Ubiquitin Edge. *Trends Mol Med* **23**,
1250 296-309 (2017).
1251
- 1252 24. Sasaki K, Iwai K. Roles of linear ubiquitylation, a crucial regulator of NF-kappaB and
1253 cell death, in the immune system. *Immunol Rev* **266**, 175-189 (2015).
1254
- 1255 25. Ikeda F. Linear ubiquitination signals in adaptive immune responses. *Immunol Rev*
1256 **266**, 222-236 (2015).
1257
- 1258 26. Iwai K, Fujita H, Sasaki Y. Linear ubiquitin chains: NF-kappaB signalling, cell death and
1259 beyond. *Nat Rev Mol Cell Biol* **15**, 503-508 (2014).
1260
- 1261 27. Maubach G, Schmadicke AC, Naumann M. NEMO Links Nuclear Factor-kappaB to
1262 Human Diseases. *Trends Mol Med* **23**, 1138-1155 (2017).
1263
- 1264 28. Clark K, Nanda S, Cohen P. Molecular control of the NEMO family of ubiquitin-binding
1265 proteins. *Nature reviews Cancer* **13**, 673-685 (2013).
1266
- 1267 29. Israel A. The IKK complex, a central regulator of NF-kappaB activation. *Cold Spring*
1268 *Harb Perspect Biol* **2**, a000158 (2010).
1269
- 1270 30. Annibaldi A, Meier P. Checkpoints in TNF-Induced Cell Death: Implications in
1271 Inflammation and Cancer. *Trends Mol Med* **24**, 49-65 (2018).
1272
- 1273 31. Brenner D, Blaser H, Mak TW. Regulation of tumour necrosis factor signalling: live or
1274 let die. *Nat Rev Immunol* **15**, 362-374 (2015).
1275
- 1276 32. Smahi A, *et al.* Genomic rearrangement in NEMO impairs NF-kappaB activation and is
1277 a cause of incontinentia pigmenti. The International Incontinentia Pigmenti (IP)
1278 Consortium. *Nature* **405**, 466-472 (2000).
1279
- 1280 33. Fusco F, *et al.* EDA-ID and IP, two faces of the same coin: how the same IKBKG/NEMO
1281 mutation affecting the NF-kappaB pathway can cause immunodeficiency and/or
1282 inflammation. *Int Rev Immunol* **34**, 445-459 (2015).
1283

- 1284 34. Conte MI, *et al.* Insight into IKBKG/NEMO locus: report of new mutations and complex
1285 genomic rearrangements leading to incontinentia pigmenti disease. *Hum Mutat* **35**,
1286 165-177 (2014).
1287
- 1288 35. Narayanan MJ, Rangasamy S, Narayanan V. Incontinentia pigmenti (Bloch-Sulzberger
1289 syndrome). *Handb Clin Neurol* **132**, 271-280 (2015).
1290
- 1291 36. Cammarata-Scalisi F, Fusco F, Ursini MV. Incontinentia Pigmenti. *Actas Dermosifiliogr*
1292 (*Engl Ed*) **110**, 273-278 (2019).
1293
- 1294 37. van Well EM, *et al.* A protein quality control pathway regulated by linear ubiquitination.
1295 *EMBO J* **38**, (2019).
1296
- 1297 38. Goel S, *et al.* Linear ubiquitination induces NEMO phase separation to activate NF-
1298 kappaB signaling. *Life Sci Alliance* **6**, (2023).
1299
- 1300 39. Gupta R, *et al.* Firefly luciferase mutants as sensors of proteome stress. *Nat Methods*
1301 **8**, 879-884 (2011).
1302
- 1303 40. Blumenstock S, *et al.* Fluc-EGFP reporter mice reveal differential alterations of
1304 neuronal proteostasis in aging and disease. *EMBO J* **40**, e107260 (2021).
1305
- 1306 41. Polinski NK, *et al.* Best Practices for Generating and Using Alpha-Synuclein Pre-
1307 Formed Fibrils to Model Parkinson's Disease in Rodents. *J Parkinsons Dis* **8**, 303-322
1308 (2018).
1309
- 1310 42. Volpicelli-Daley LA, Luk KC, Lee VM. Addition of exogenous alpha-synuclein
1311 preformed fibrils to primary neuronal cultures to seed recruitment of endogenous alpha-
1312 synuclein to Lewy body and Lewy neurite-like aggregates. *Nat Protoc* **9**, 2135-2146
1313 (2014).
1314
- 1315 43. Trinkaus VA, *et al.* In situ architecture of neuronal alpha-Synuclein inclusions. *Nat*
1316 *Commun* **12**, 2110 (2021).
1317
- 1318 44. Matsumoto ML, *et al.* Engineering and structural characterization of a linear
1319 polyubiquitin-specific antibody. *J Mol Biol* **418**, 134-144 (2012).
1320

- 1321 45. Tokunaga F, *et al.* Involvement of linear polyubiquitylation of NEMO in NF-kappaB
1322 activation. *Nat Cell Biol* **11**, 123-132 (2009).
1323
- 1324 46. Fujita H, *et al.* Mechanism underlying IkappaB kinase activation mediated by the linear
1325 ubiquitin chain assembly complex. *Mol Cell Biol* **34**, 1322-1335 (2014).
1326
- 1327 47. Rahighi S, Iyer M, Oveisi H, Nasser S, Duong V. Structural basis for the simultaneous
1328 recognition of NEMO and acceptor ubiquitin by the HOIP NZF1 domain. *Sci Rep* **12**,
1329 12241 (2022).
1330
- 1331 48. Noad J, von der Malsburg A, Pathe C, Michel MA, Komander D, Randow F. LUBAC-
1332 synthesized linear ubiquitin chains restrict cytosol-invading bacteria by activating
1333 autophagy and NF-kappaB. *Nat Microbiol* **2**, 17063 (2017).
1334
- 1335 49. van Wijk SJL, *et al.* Linear ubiquitination of cytosolic Salmonella Typhimurium activates
1336 NF-kappaB and restricts bacterial proliferation. *Nat Microbiol* **2**, 17066 (2017).
1337
- 1338 50. Otten EG, *et al.* Ubiquitylation of lipopolysaccharide by RNF213 during bacterial
1339 infection. *Nature* **594**, 111-116 (2021).
1340
- 1341 51. Stefanis L, Emmanouilidou E, Pantazopoulou M, Kirik D, Vekrellis K, Tofaris GK. How
1342 is alpha-synuclein cleared from the cell? *J Neurochem* **150**, 577-590 (2019).
1343
- 1344 52. Sahoo S, Padhy AA, Kumari V, Mishra P. Role of Ubiquitin-Proteasome and
1345 Autophagy-Lysosome Pathways in alpha-Synuclein Aggregate Clearance. *Mol*
1346 *Neurobiol* **59**, 5379-5407 (2022).
1347
- 1348 53. Lashuel HA, Overk CR, Oueslati A, Masliah E. The many faces of alpha-synuclein:
1349 from structure and toxicity to therapeutic target. *Nat Rev Neurosci* **14**, 38-48 (2013).
1350
- 1351 54. Hubeau M, *et al.* New mechanism of X-linked anhidrotic ectodermal dysplasia with
1352 immunodeficiency: impairment of ubiquitin binding despite normal folding of NEMO
1353 protein. *Blood* **118**, 926-935 (2011).
1354
- 1355 55. Rahighi S, *et al.* Specific recognition of linear ubiquitin chains by NEMO is important
1356 for NF-kappaB activation. *Cell* **136**, 1098-1109 (2009).
1357

- 1358 56. Lamark T, Svenning S, Johansen T. Regulation of selective autophagy: the
1359 p62/SQSTM1 paradigm. *Essays Biochem* **61**, 609-624 (2017).
1360
- 1361 57. Bjorkoy G, *et al.* p62/SQSTM1 forms protein aggregates degraded by autophagy and
1362 has a protective effect on huntingtin-induced cell death. *J Cell Biol* **171**, 603-614 (2005).
1363
- 1364 58. Pankiv S, *et al.* p62/SQSTM1 binds directly to Atg8/LC3 to facilitate degradation of
1365 ubiquitinated protein aggregates by autophagy. *J Biol Chem* **282**, 24131-24145 (2007).
1366
- 1367 59. Danieli A, Martens S. p62-mediated phase separation at the intersection of the
1368 ubiquitin-proteasome system and autophagy. *J Cell Sci* **131**, (2018).
1369
- 1370 60. Wurzer B, *et al.* Oligomerization of p62 allows for selection of ubiquitinated cargo and
1371 isolation membrane during selective autophagy. *eLife* **4**, e08941 (2015).
1372
- 1373 61. Zotti T, *et al.* TRAF6-mediated ubiquitination of NEMO requires p62/sequestosome-1.
1374 *Mol Immunol* **58**, 27-31 (2014).
1375
- 1376 62. Martin P, Diaz-Meco MT, Moscat J. The signaling adapter p62 is an important mediator
1377 of T helper 2 cell function and allergic airway inflammation. *Embo J* **25**, 3524-3533
1378 (2006).
1379
- 1380 63. Kuusisto E, Salminen A, Alafuzoff I. Ubiquitin-binding protein p62 is present in neuronal
1381 and glial inclusions in human tauopathies and synucleinopathies. *Neuroreport* **12**,
1382 2085-2090 (2001).
1383
- 1384 64. Trejo-Lopez JA, *et al.* Generation and Characterization of Novel Monoclonal Antibodies
1385 Targeting p62/sequestosome-1 Across Human Neurodegenerative Diseases. *J*
1386 *Neuropathol Exp Neurol* **79**, 407-418 (2020).
1387
- 1388 65. Turco E, *et al.* Reconstitution defines the roles of p62, NBR1 and TAX1BP1 in ubiquitin
1389 condensate formation and autophagy initiation. *Nat Commun* **12**, 5212 (2021).
1390
- 1391 66. Turco E, *et al.* FIP200 Claw Domain Binding to p62 Promotes Autophagosome
1392 Formation at Ubiquitin Condensates. *Mol Cell* **74**, 330-346 e311 (2019).
1393

- 1394 67. Sun D, Wu R, Zheng J, Li P, Yu L. Polyubiquitin chain-induced p62 phase separation
1395 drives autophagic cargo segregation. *Cell Res* **28**, 405-415 (2018).
1396
- 1397 68. Zaffagnini G, *et al.* p62 filaments capture and present ubiquitinated cargos for
1398 autophagy. *EMBO J* **37**, (2018).
1399
- 1400 69. Jakobi AJ, *et al.* Structural basis of p62/SQSTM1 helical filaments and their role in
1401 cellular cargo uptake. *Nat Commun* **11**, 440 (2020).
1402
- 1403 70. Du M, Ea CK, Fang Y, Chen ZJ. Liquid phase separation of NEMO induced by
1404 polyubiquitin chains activates NF-kappaB. *Mol Cell*, (2022).
1405
- 1406 71. Yamasaki A, *et al.* Liquidity Is a Critical Determinant for Selective Autophagy of Protein
1407 Condensates. *Mol Cell* **77**, 1163-1175 e1169 (2020).
1408
- 1409 72. Gallagher ER, Holzbaur ELF. The selective autophagy adaptor p62/SQSTM1 forms
1410 phase condensates regulated by HSP27 that facilitate the clearance of damaged
1411 lysosomes via lysophagy. *Cell Rep* **42**, 112037 (2023).
1412
- 1413 73. Ma X, Zhang M, Ge L. A switch of chaperonin function regulates the clearance of solid
1414 protein aggregates. *Autophagy* **18**, 2746-2748 (2022).
1415
- 1416 74. Peng SZ, *et al.* Phase separation of Nur77 mediates celastrol-induced mitophagy by
1417 promoting the liquidity of p62/SQSTM1 condensates. *Nat Commun* **12**, 5989 (2021).
1418
- 1419 75. Kageyama S, *et al.* p62/SQSTM1-droplet serves as a platform for autophagosome
1420 formation and anti-oxidative stress response. *Nat Commun* **12**, 16 (2021).
1421
- 1422 76. Jain A, *et al.* p62/SQSTM1 is a target gene for transcription factor NRF2 and creates a
1423 positive feedback loop by inducing antioxidant response element-driven gene
1424 transcription. *J Biol Chem* **285**, 22576-22591 (2010).
1425
- 1426 77. Tusco R, *et al.* Kenny mediates selective autophagic degradation of the IKK complex
1427 to control innate immune responses. *Nat Commun* **8**, 1264 (2017).
1428
- 1429 78. Meffert MK, Chang JM, Wiltgen BJ, Fanselow MS, Baltimore D. NF-kappa B functions
1430 in synaptic signaling and behavior. *Nat Neurosci* **6**, 1072-1078 (2003).

1431

1432 79. Neidl R, *et al.* Late-Life Environmental Enrichment Induces Acetylation Events and
1433 Nuclear Factor kappaB-Dependent Regulations in the Hippocampus of Aged Rats
1434 Showing Improved Plasticity and Learning. *J Neurosci* **36**, 4351-4361 (2016).

1435

1436 80. O'Riordan KJ, *et al.* Regulation of nuclear factor kappaB in the hippocampus by group
1437 I metabotropic glutamate receptors. *J Neurosci* **26**, 4870-4879 (2006).

1438

1439 81. Dresselhaus EC, Boersma MCH, Meffert MK. Targeting of NF-kappaB to Dendritic
1440 Spines Is Required for Synaptic Signaling and Spine Development. *J Neurosci* **38**,
1441 4093-4103 (2018).

1442

1443 82. Bhakar AL, *et al.* Constitutive nuclear factor-kappa B activity is required for central
1444 neuron survival. *J Neurosci* **22**, 8466-8475 (2002).

1445

1446 83. Blondeau N, Widmann C, Lazdunski M, Heurteaux C. Activation of the nuclear factor-
1447 kappaB is a key event in brain tolerance. *J Neurosci* **21**, 4668-4677 (2001).

1448

1449 84. Cheng B, Christakos S, Mattson MP. Tumor necrosis factors protect neurons against
1450 metabolic-excitotoxic insults and promote maintenance of calcium homeostasis.
1451 *Neuron* **12**, 139-153 (1994).

1452

1453 85. Turrin NP, Rivest S. Tumor necrosis factor alpha but not interleukin 1 beta mediates
1454 neuroprotection in response to acute nitric oxide excitotoxicity. *J Neurosci* **26**, 143-151
1455 (2006).

1456

1457 86. Carter BD, *et al.* Selective activation of NF-kappa B by nerve growth factor through the
1458 neurotrophin receptor p75. *Science* **272**, 542-545 (1996).

1459

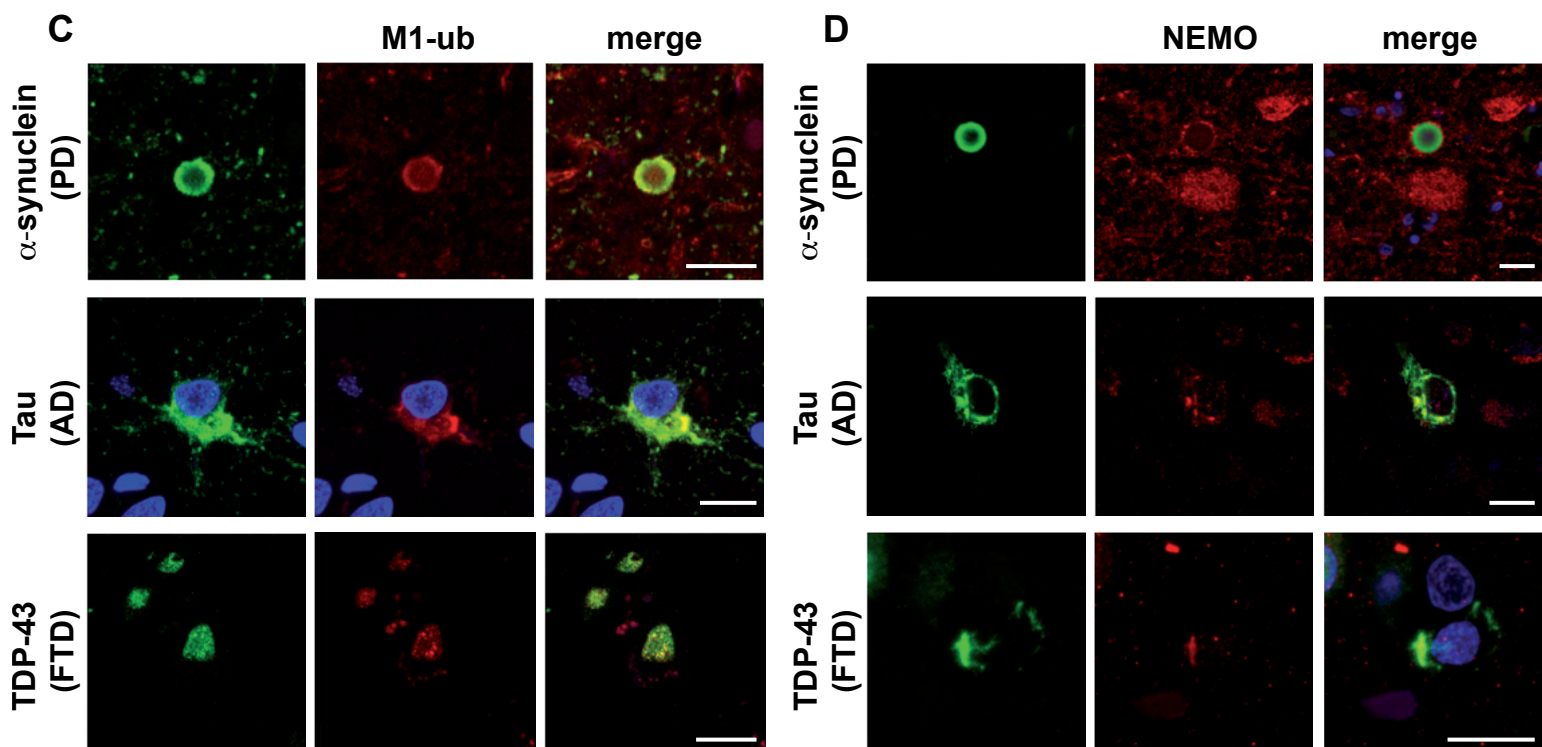
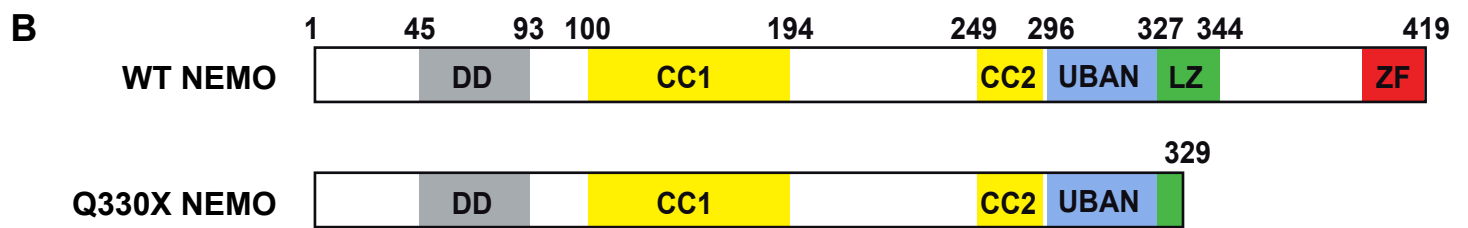
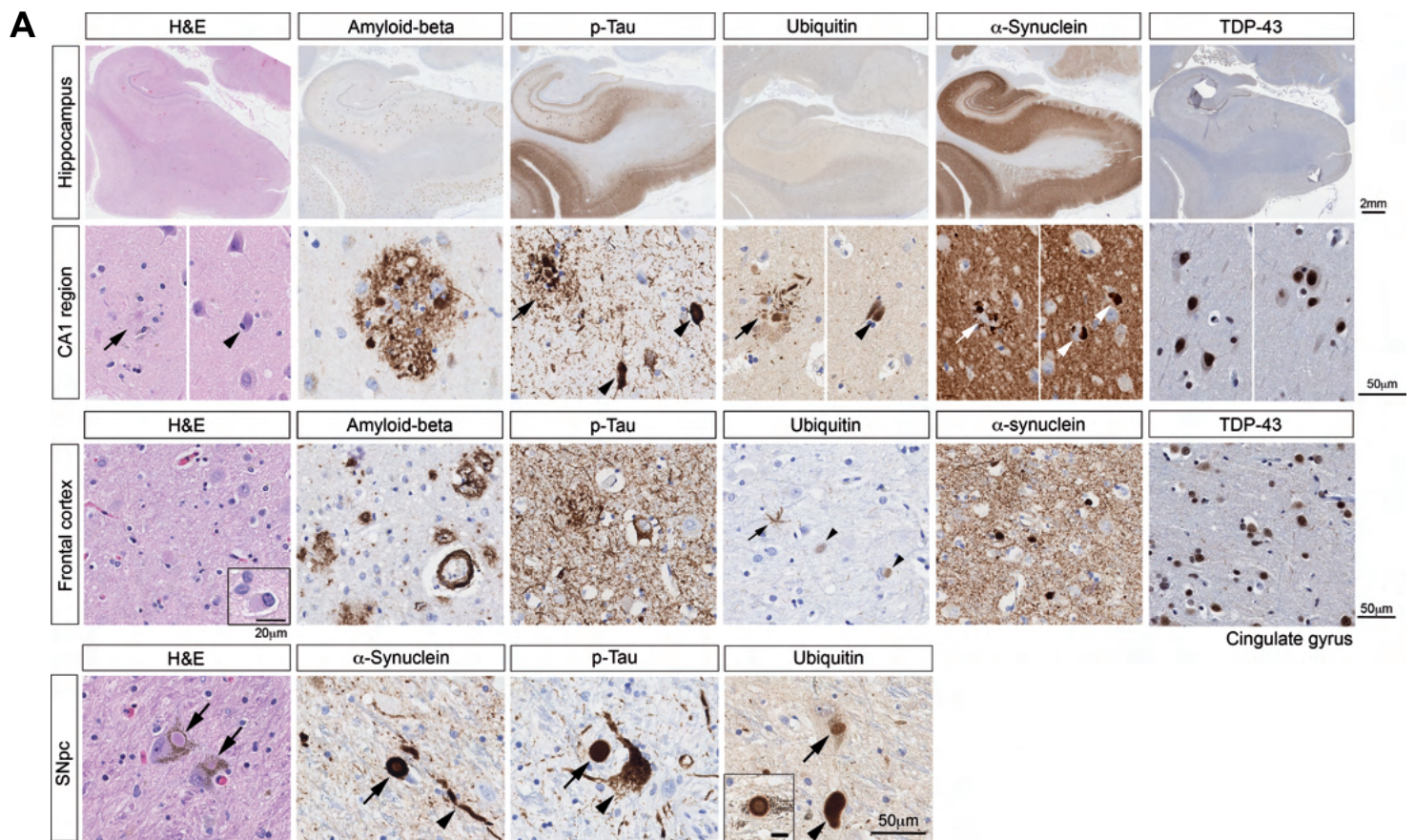
1460 87. Foehr ED, Lin X, O'Mahony A, Geleziunas R, Bradshaw RA, Greene WC. NF-kappa B
1461 signaling promotes both cell survival and neurite process formation in nerve growth
1462 factor-stimulated PC12 cells. *J Neurosci* **20**, 7556-7563 (2000).

1463

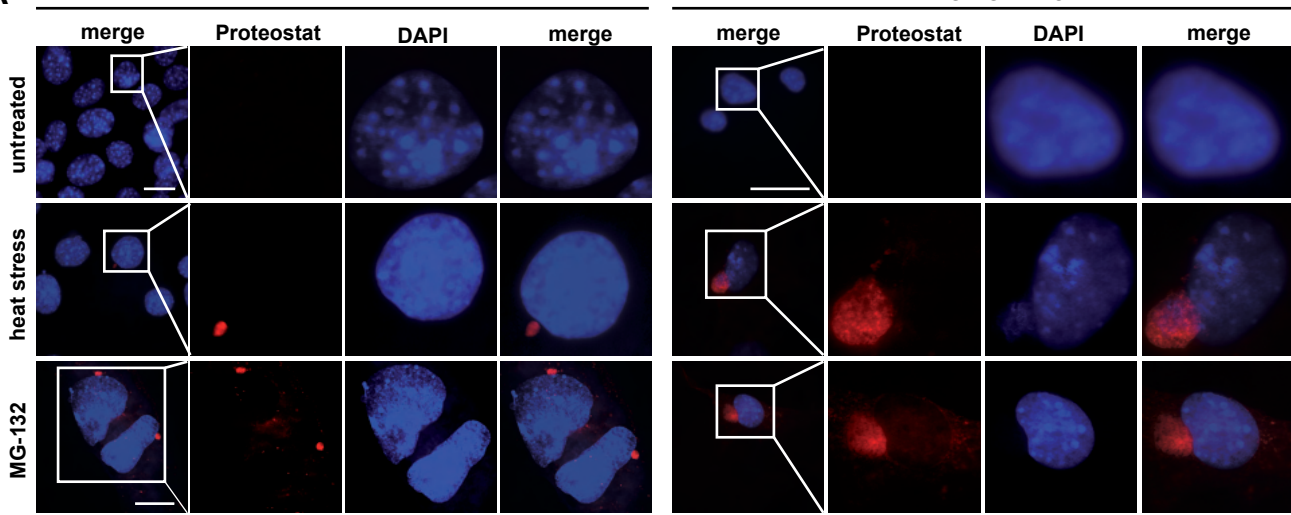
1464 88. Nakajima K, *et al.* Neurotrophins regulate the function of cultured microglia. *Glia* **24**,
1465 272-289 (1998).

1466

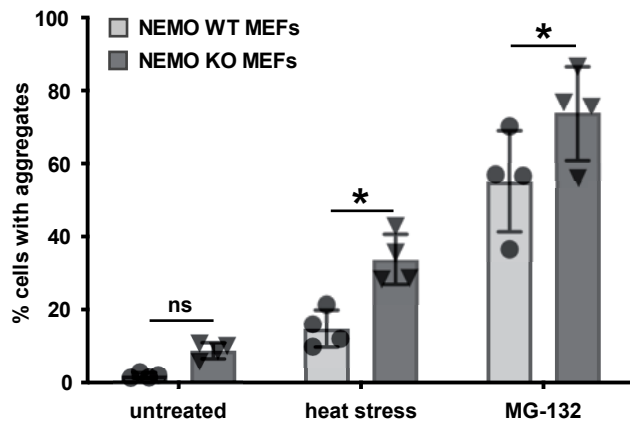
- 1467 89. Hayashi H, *et al.* Characterization of intracellular signals via tyrosine 1062 in RET
1468 activated by glial cell line-derived neurotrophic factor. *Oncogene* **19**, 4469-4475 (2000).
1469
- 1470 90. Meka DP, *et al.* Parkin cooperates with GDNF/RET signaling to prevent dopaminergic
1471 neuron degeneration. *J Clin Invest* **125**, 1873-1885 (2015).
1472
- 1473 91. Muller-Rischart AK, *et al.* The E3 ligase parkin maintains mitochondrial integrity by
1474 increasing linear ubiquitination of NEMO. *Mol Cell* **49**, 908-921 (2013).
1475
- 1476 92. Henn IH, *et al.* Parkin mediates neuroprotection through activation of I κ B
1477 kinase/nuclear factor- κ B signaling. *J Neurosci* **27**, 1868-1878 (2007).
1478
- 1479 93. Ayaki T, *et al.* Multiple Proteinopathies in Familial ALS Cases With Optineurin
1480 Mutations. *J Neuropathol Exp Neurol* **77**, 128-138 (2018).
1481
- 1482 94. Schmidt-Supprian M, *et al.* NEMO/IKK gamma-deficient mice model incontinentia
1483 pigmenti. *Mol Cell* **5**, 981-992 (2000).
1484
- 1485 95. Komatsu M, *et al.* Homeostatic levels of p62 control cytoplasmic inclusion body
1486 formation in autophagy-deficient mice. *Cell* **131**, 1149-1163 (2007).
1487
1488



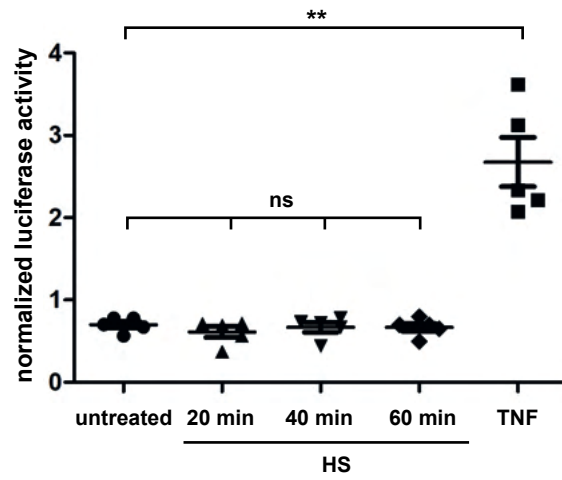
A



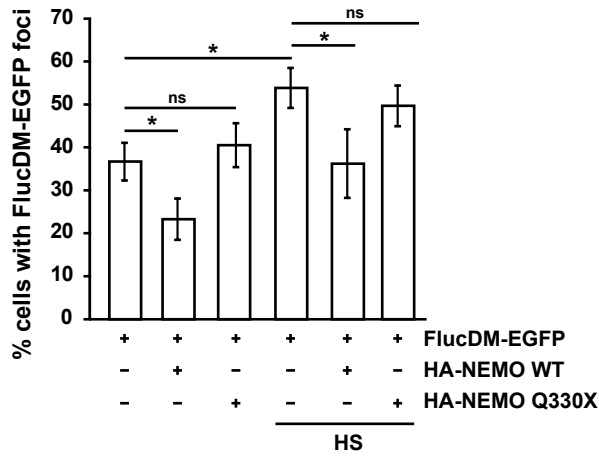
B



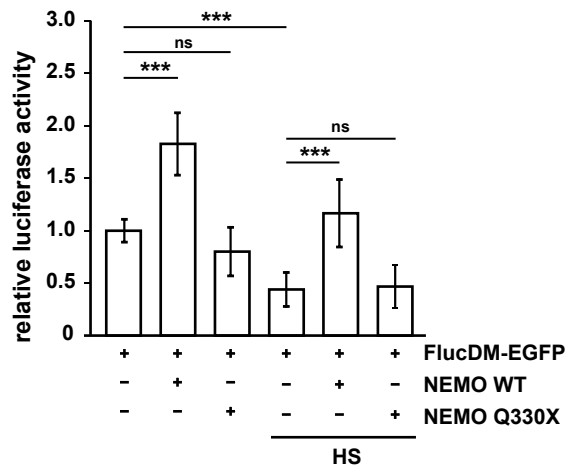
E



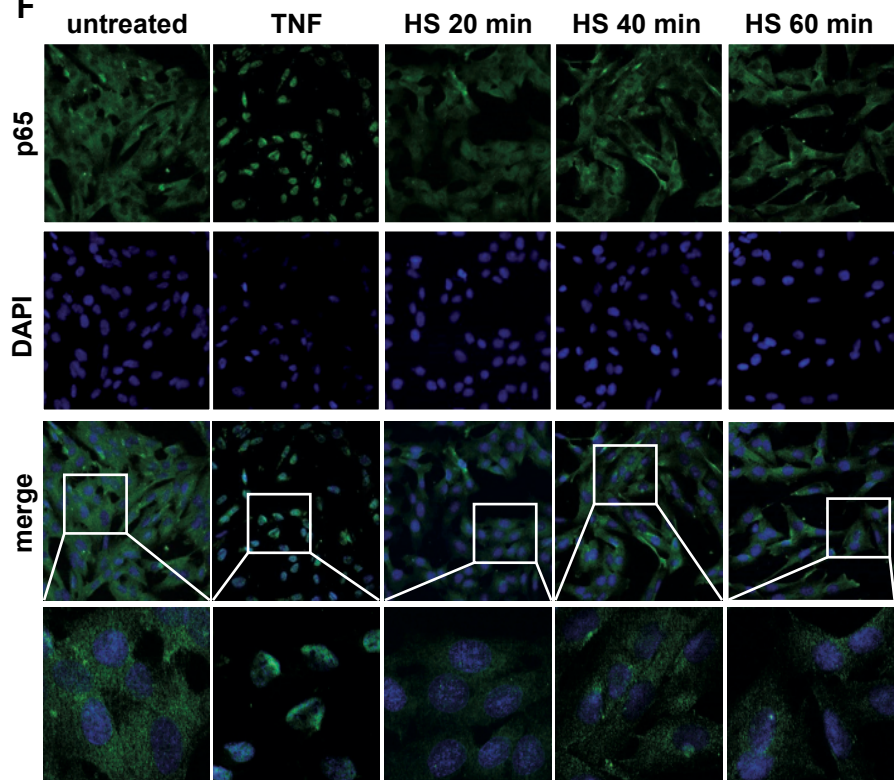
C

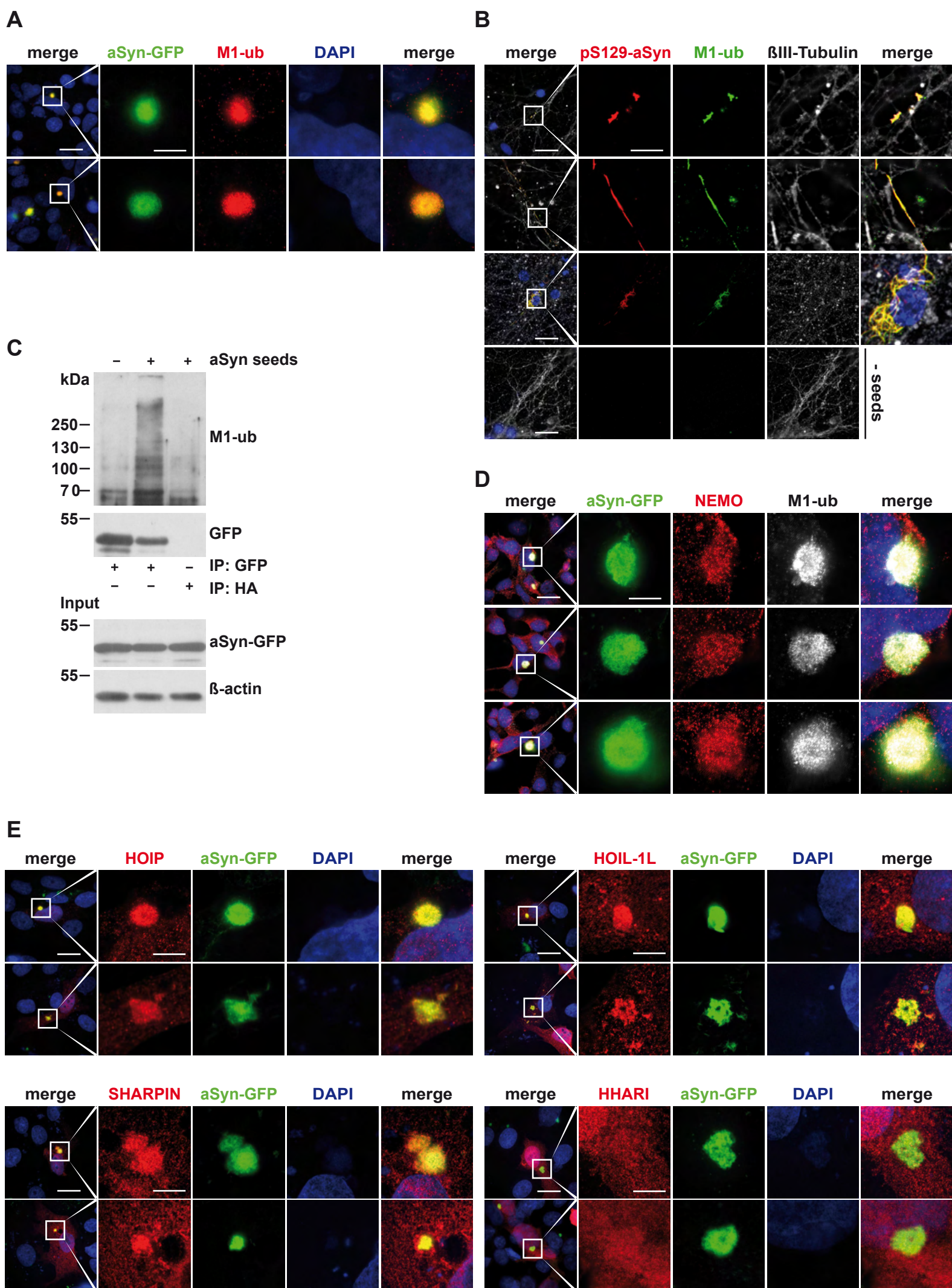


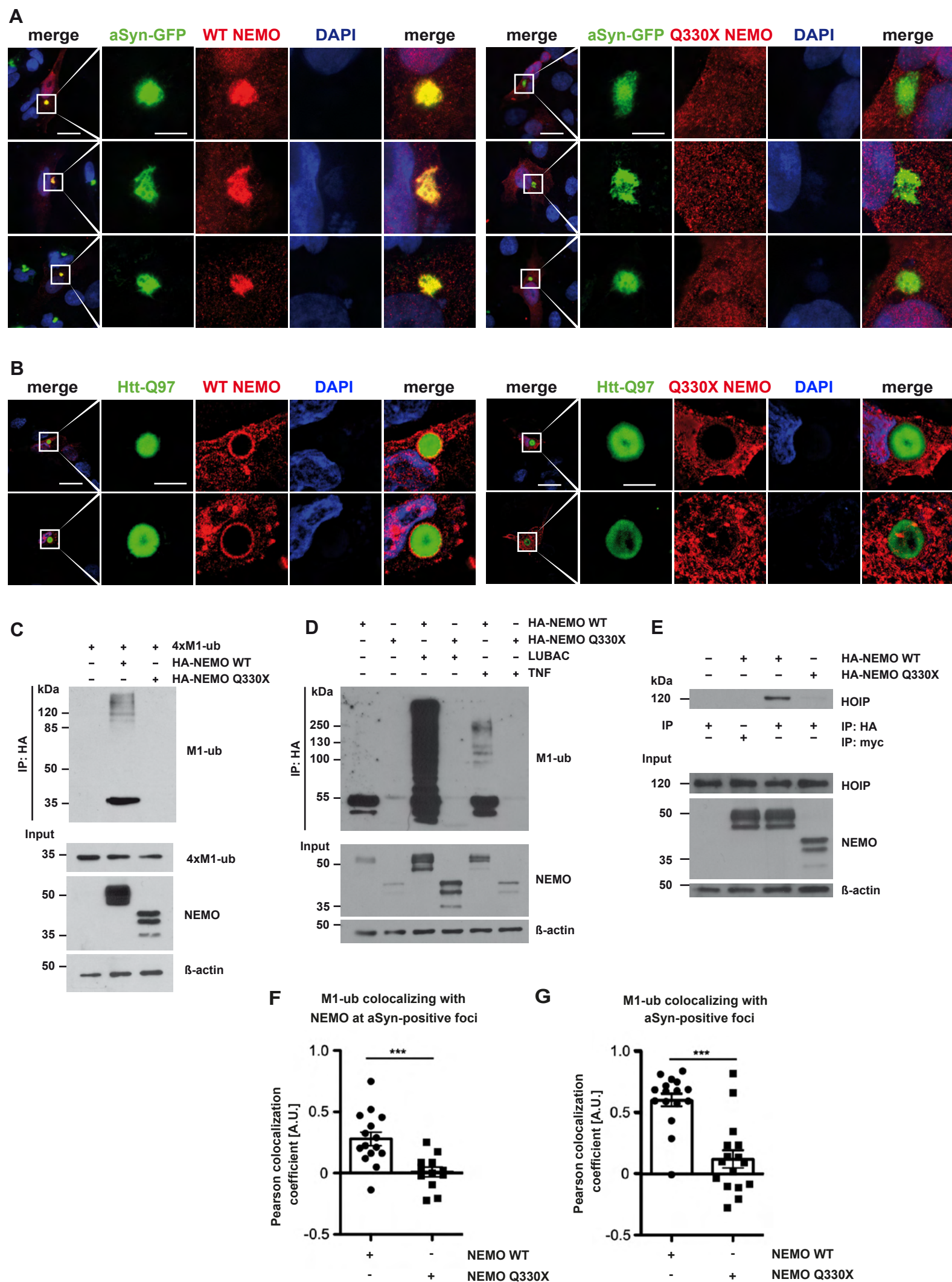
D



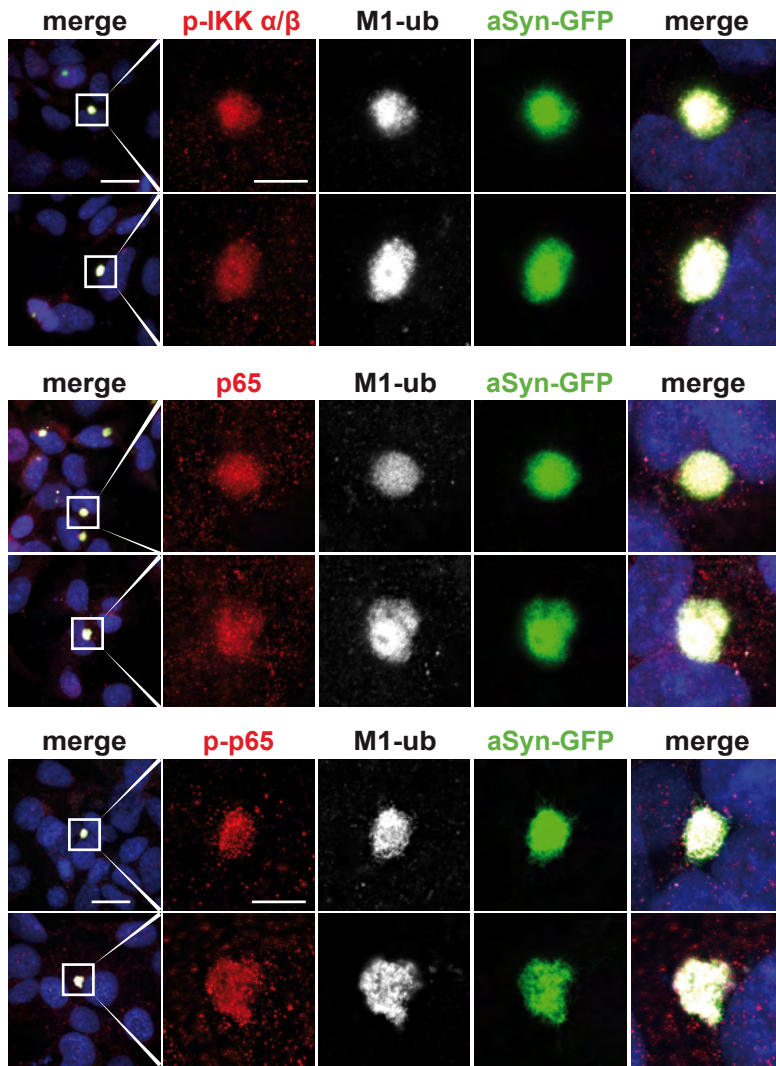
F



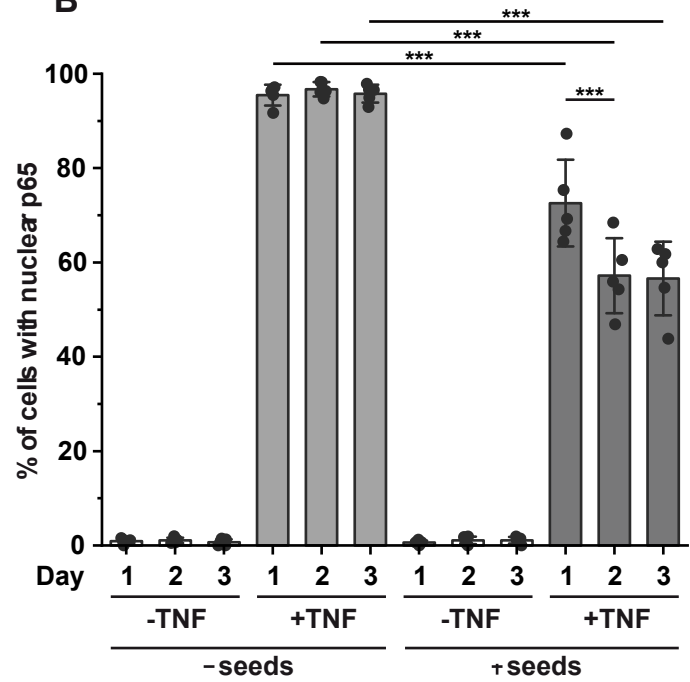




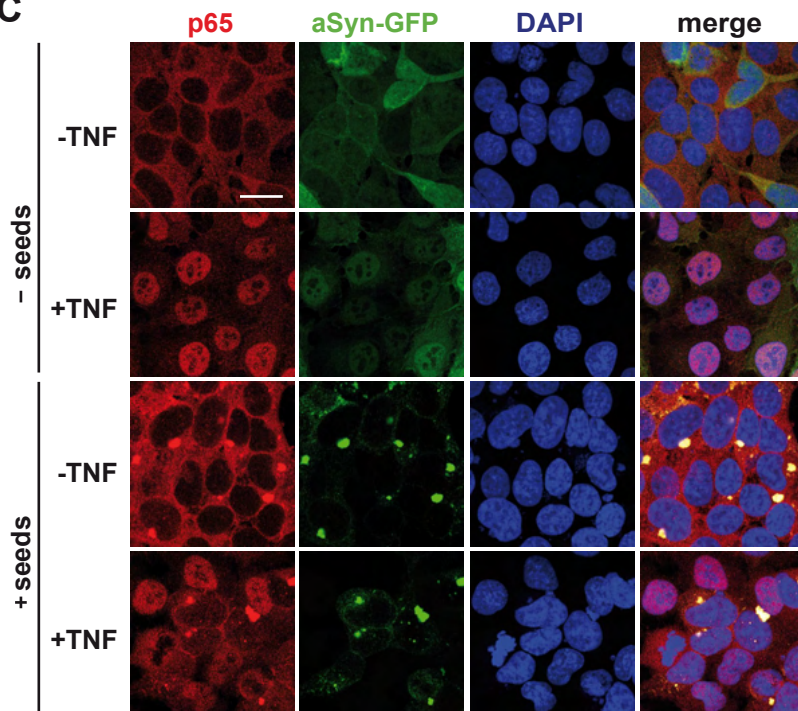
A



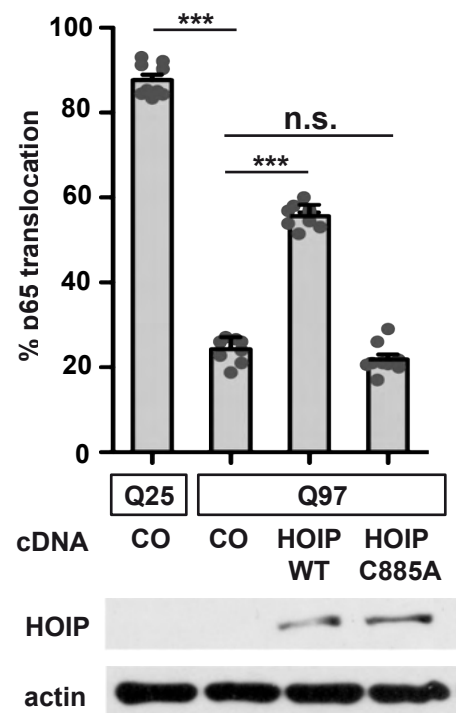
B



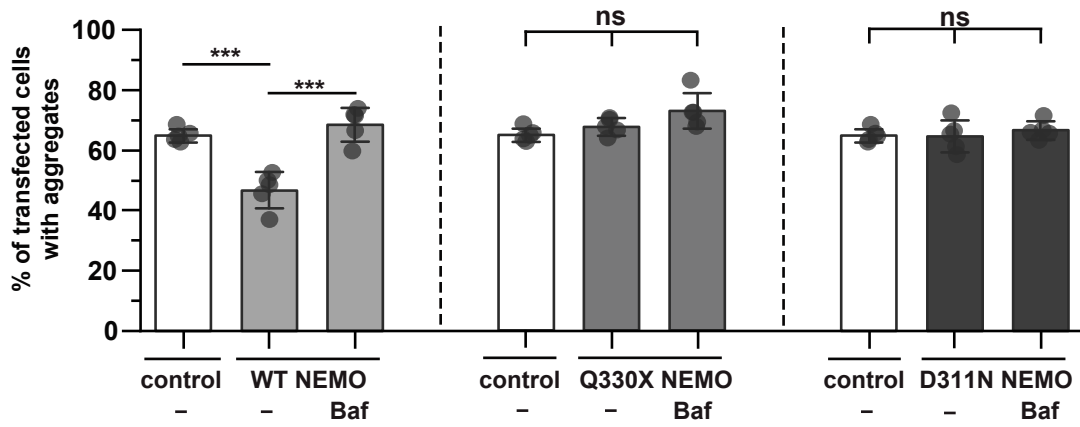
C



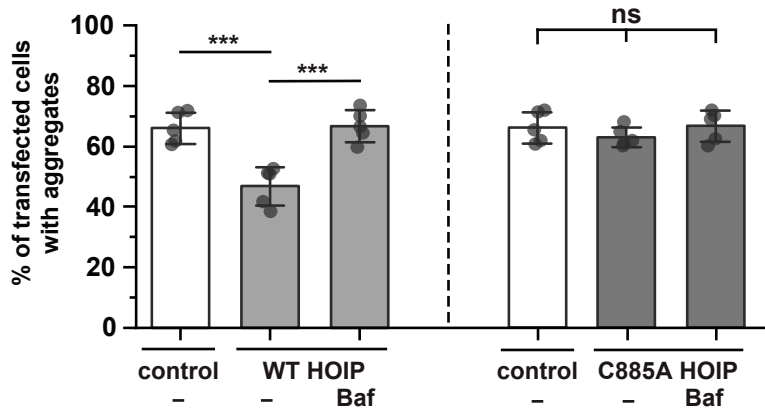
D



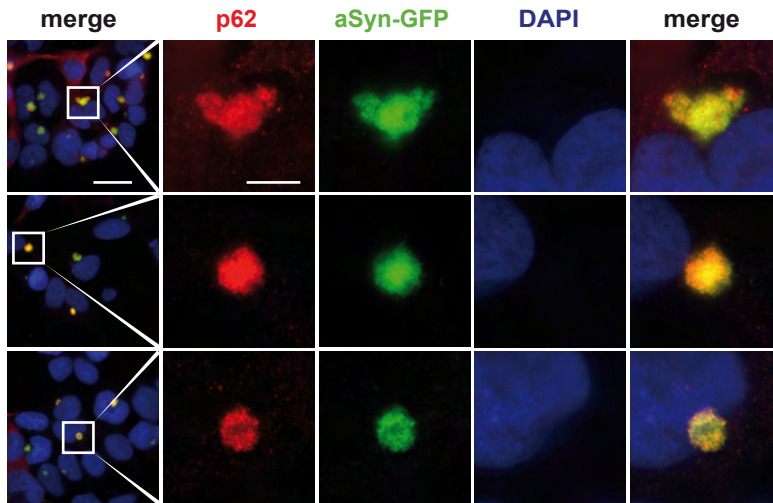
A



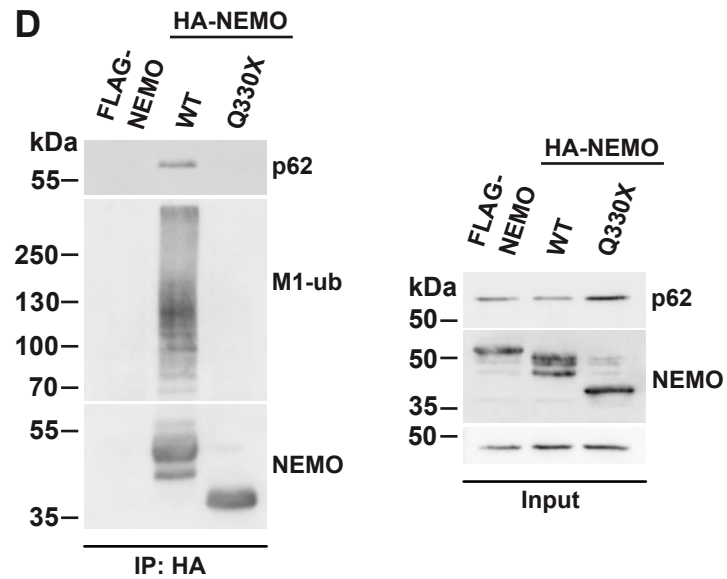
B



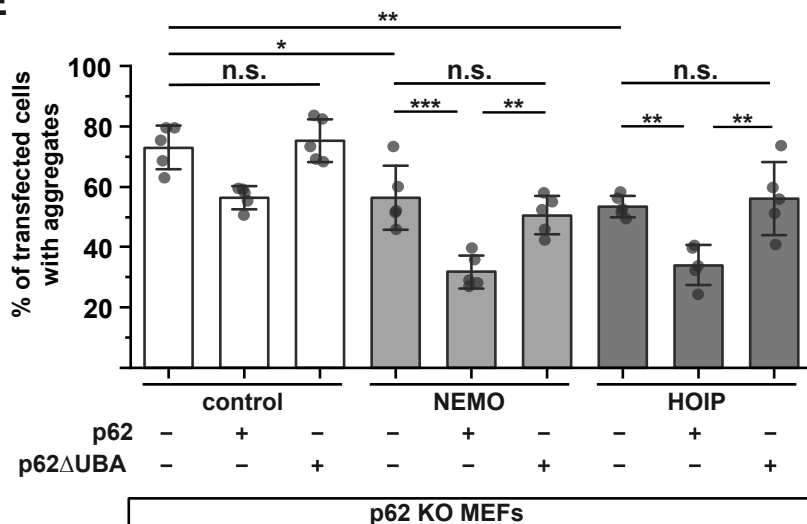
C



D



E



F

